

# The Roles Potassium Currents Play in Regulating the Electrical Activity of Ventral Cochlear Nucleus Neurons

Jason S. Rothman<sup>1</sup> and Paul B. Manis<sup>2</sup>

*The Center for Hearing Science, <sup>1</sup>Department of Biomedical Engineering, The Johns Hopkins University School of Medicine, Baltimore, Maryland 21205; and <sup>2</sup>Department of Otolaryngology/Head and Neck Surgery, and The Curriculum in Neurobiology, University of North Carolina, Chapel Hill, North Carolina 27599*

**Rothman, Jason S. and Paul B. Manis.** The roles potassium currents play in regulating the electrical activity of ventral cochlear nucleus neurons. *J Neurophysiol* 89: 3097–3113, 2003; 10.1152/jn.00127.2002. Using kinetic data from three different K<sup>+</sup> currents in acutely isolated neurons, a single electrical compartment representing the soma of a ventral cochlear nucleus (VCN) neuron was created. The K<sup>+</sup> currents include a fast transient current ( $I_A$ ), a slow-inactivating low-threshold current ( $I_{LT}$ ), and a noninactivating high-threshold current ( $I_{HT}$ ). The model also includes a fast-inactivating Na<sup>+</sup> current, a hyperpolarization-activated cation current ( $I_h$ ), and 1–50 auditory nerve synapses. With this model, the role  $I_A$ ,  $I_{LT}$ , and  $I_{HT}$  play in shaping the discharge patterns of VCN cells is explored. Simulation results indicate that  $I_{HT}$  mainly functions to repolarize the membrane during an action potential, and  $I_A$  functions to modulate the rate of repetitive firing.  $I_{LT}$  is found to be responsible for the phasic discharge pattern observed in Type II cells (bushy cells). However, by adjusting the strength of  $I_{LT}$ , both phasic and regular discharge patterns are observed, demonstrating that a critical level of  $I_{LT}$  is necessary to produce the Type II response. Simulated Type II cells have a significantly faster membrane time constant in comparison to Type I cells (stellate cells) and are therefore better suited to preserve temporal information in their auditory nerve inputs by acting as precise coincidence detectors and having a short refractory period. Finally, we demonstrate that modulation of  $I_h$ , which changes the resting membrane potential, is a more effective means of modulating the activation level of  $I_{LT}$  than simply modulating  $I_{LT}$  itself. This result may explain why  $I_{LT}$  and  $I_h$  are often coexpressed throughout the nervous system.

## INTRODUCTION

A major goal of studying neuronal mechanisms of information processing is to determine precisely how each mechanism contributes to the electrical activity of a neuron. Because voltage-gated ionic currents introduce strong nonlinearities into a cell's electrical behavior, computational models are often necessary to provide the appropriate predictive power. In our previous papers, we provided a detailed description of three K<sup>+</sup> currents expressed across a population of ventral cochlear nucleus (VCN) neurons (Rothman and Manis 2003a,b). The measurements from these currents allowed us to create kinetic models of VCN neurons with a precision not previously available.

Several models of VCN stellate and bushy cells have already been described. Banks and Sachs (1991), for example, pre-

sented a stellate cell model consisting of an active somatic and axonal compartment coupled to a passive dendritic tree. Because little was known about the Na<sup>+</sup> and K<sup>+</sup> currents in VCN stellate cells before 1991, Banks and Sachs used modified versions of the Hodgkin and Huxley (HH) equations (1952), which included a fast Na<sup>+</sup> current ( $I_{Na}$ ) and a high-threshold K<sup>+</sup> current ( $I_{HT}$ ). Wang and Sachs (1995) presented a modified version of the Banks and Sachs stellate cell model where, to account for a higher spike threshold observed in vitro, the activation curves of  $I_{Na}$  and  $I_{HT}$  were shifted 10 mV positive. Arle and Kim (1991) and Hewitt et al. (1992) presented “MacGregor-type” stellate cell models in which  $I_{HT}$  was treated as a digital entity; that is, it was “on” during an action potential (AP) but “off” at other times. In general, the preceding HH-like and MacGregor-like stellate models were successful in that they replicated many of the response characteristics of stellate cells in vitro and in vivo. For example, during a depolarizing current pulse, the models exhibited repetitive firing (i.e. a Type I current-clamp response) and when stimulated with auditory-nerve-like synaptic input, the models exhibit a “chopping” response in their poststimulus time histograms (PSTHs), reflecting their regular discharge. These models were also successful in replicating responses to more complex stimuli (Arle and Kim 1991; Hewitt et al. 1992; Wang and Sachs 1995).

Models of VCN bushy cells have also been described. Rothman et al. (1993), for example, presented a model based on the voltage-clamp study of Manis and Marx (1991). Because only the low-threshold current ( $I_{LT}$ ) had been fully characterized at the time, models of  $I_{Na}$  and  $I_{HT}$  were based on those of Frankenhaeuser and Huxley (1964). Perney and Kaczmarek (1997) also presented a model of VCN bushy cells. In this case,  $I_{LT}$  was based on the data of Manis and Marx (1991) and  $I_{HT}$  was based on a study of a *Shaw* voltage-activated K<sup>+</sup> channel (KCNC1) expressed in NIH 3T3 fibroblasts (Kanemasa et al. 1995) because KCNC1 is thought to be a component of the delayed rectifier in VCN neurons (Perney and Kaczmarek 1997). Like the stellate cell models, these bushy cell models successfully replicated many of the response characteristics of bushy cells in vitro and in vivo, including a phasic discharge of APs in response to a depolarizing current pulse (i.e. a Type II current-clamp response) and the ability to follow a train of

Address for reprint requests: Paul B. Manis, Dept. Otolaryngology/Head and Neck Surgery, 1123 Bioinformatics Bldg., CB#7070, The University of North Carolina at Chapel Hill, Chapel Hill, NC 27599-7070 (E-mail: pmanis@med.unc.edu).

The costs of publication of this article were defrayed in part by the payment of page charges. The article must therefore be hereby marked “advertisement” in accordance with 18 U.S.C. Section 1734 solely to indicate this fact.

auditory-nerve-like synaptic inputs at relatively high frequencies.

Although these models have generally been successful in replicating the response characteristics of stellate and bushy cells, they were developed on the basis of incomplete information regarding the  $K^+$  channels. Figure 1 compares the voltage dependence and kinetics of some of the  $K^+$  currents used in previous models. In this figure, normalized activation functions, whole cell currents, and time constants of the model "high-threshold" currents are plotted on the *left* ( $n^\lambda$ ,  $I_{HT}$ , and  $\tau_n$ ), and those of the model "low-threshold" currents are plotted on the *right* ( $w^\lambda$ ,  $I_{LT}$ , and  $\tau_w$ ). The thin lines correspond to the models, and the bold lines pertain to the mean experimental data presented in our previous studies (Rothman and Manis 2003a,b). Not included in this figure are the MacGregor-type models because these models have unrealistic  $K^+$  currents in

that they turn on and off instantaneously. Comparison between the model and experimental data reveals several discrepancies. First, the activation functions of the model high-threshold currents ( $n^\lambda$ ) all show significant deviation from the experimental data in that they have shallow voltage dependencies and activate over different voltage ranges. When these activation functions are converted into whole cell currents ( $I_{HT}$ ), the discrepancies become even more pronounced (note y axis log scaling). All of the descriptions show significant activation for potentials just above rest: their activation thresholds ( $V_{th}$ ) fall between  $-52$  and  $-62$  mV. According to our experimental data (Rothman and Manis 2003a), such currents would be classified not as high threshold but low threshold. Indeed, one  $I_{HT}$  model with  $V_{th}$  near  $-60$  mV (Perney and Kaczmarek 1997) used a large value for its total conductance ( $50 \mu S$ ; Fig. 1, trace 2), and consequently behaves entirely like  $I_{LT}$ . For the bushy cell models, this means activation of  $I_{HT}$  overlaps that of  $I_{LT}$  and therefore contributes to the proposed effects of  $I_{LT}$ . For the stellate cell models, this means their intrinsic membrane properties (i.e. input resistance and membrane time constant) are more similar to those of bushy cells than stellate cells.

The second discrepancy in Fig. 1 pertains to  $I_{LT}$ : the magnitudes of the model currents are approximately 10 times smaller than indicated by the new experimental data. Thus the full extent of the  $I_{LT}$ 's ability to reduce the membrane time constant was not fully explored in the previous models.

The last two discrepancies in Fig. 1 pertain to the time constants of  $I_{HT}$  ( $\tau_n$ ) and  $I_{LT}$  ( $\tau_w$ ). For  $\tau_n$ , discrepancies occur at potentials less than  $-60$  mV. For  $\tau_w$ , discrepancies occur at all potentials. Although the discrepancies in time constants probably do not lead to dramatic differences in membrane properties at suprathreshold potentials (i.e. during an action potential), they could have subtle effects on membrane properties at subthreshold potentials, such as refractoriness.

Hence, given the many discrepancies between the previous models and our new experimental data, we thought it important and necessary to theoretically reexamine the roles  $K^+$  currents play in regulating the electrical activity of VCN neurons.

## METHODS

### VCN somatic model

The VCN model described in this paper consists of a single electrical compartment with a membrane capacitance ( $C_m$ ) connected in parallel with a fast-inactivating A-type  $K^+$  current ( $I_A$ ), a fast-activating slow-inactivating low-threshold  $K^+$  current ( $I_{LT}$ ), a high-threshold  $K^+$  current ( $I_{HT}$ ), a fast-inactivating TTX-sensitive  $Na^+$  current ( $I_{Na}$ ), a hyperpolarization-activated cation current ( $I_h$ ), a leakage current ( $I_{lk}$ ), an excitatory synaptic current ( $I_E$ ), and an external electrode current source ( $I_{ext}$ ). For such an electrical circuit, the membrane potential  $V$  is described by the following first-order differential equation

$$C_m \frac{dV}{dt} = I_A + I_{LT} + I_{HT} + I_{Na} + I_h + I_{lk} + I_E - I_{ext} \quad (1)$$

Equations for  $I_A$ ,  $I_{LT}$  and  $I_{HT}$  were derived from experimental data, as previously described (Rothman and Manis 2003b), and are collectively given in the APPENDIX. Because  $I_{Na}$  and  $I_h$  were not studied in our voltage-clamp experiments, their models were derived from other studies, as described in the following text. Equations for  $I_{lk}$  and  $I_E$  are also described in the following text. Except for the current-clamp simulations,  $I_{ext} = 0$ . For all simulations,  $C_m = 12$  pF, the average

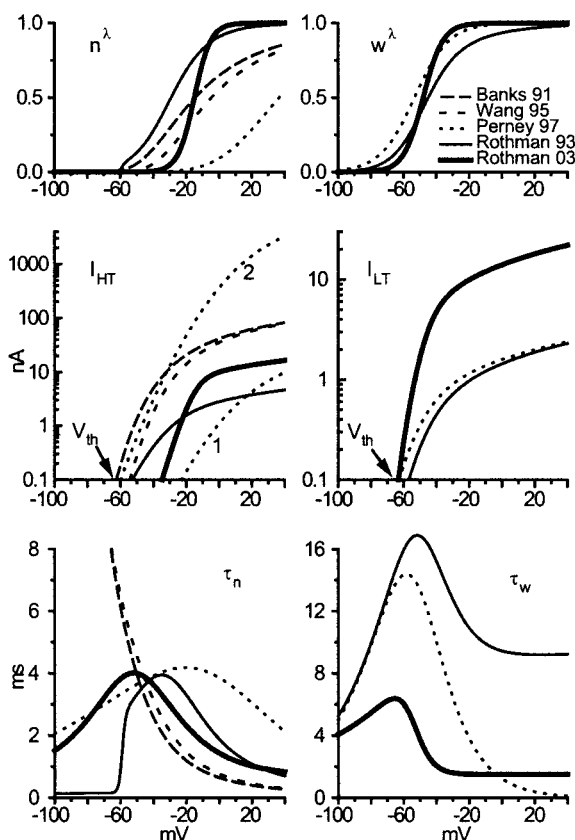


FIG. 1. Comparison of model ventral cochlear nucleus (VCN)  $K^+$  currents. Normalized activation functions, whole cell currents, and time constants of model "high-threshold" currents ( $n^\lambda$ ,  $I_{HT}$ ,  $\tau_n$ ) and "low-threshold" currents ( $w^\lambda$ ,  $I_{LT}$ ,  $\tau_w$ ). Thin lines represent each model, and bold lines represent the experimental data presented in our previous study (Rothman and Manis 2003b) as well as the VCN model described in this study. For the Banks and Sachs stellate cell model (1991, long dashed line) and the Wang and Sachs stellate cell model (1995) (short dashed line),  $n^\lambda$  is their  $n_\infty^4$ . For the Rothman et al. bushy cell model (1993) (thin line),  $n^\lambda$  is their  $n_\infty$ , and  $w^\lambda$  is their  $w_\infty$ . For the Perney and Kaczmarek bushy cell model (1997) (dotted line),  $n^\lambda$  is their  $(0.6n_\infty^4 - 0.4p_\infty n_\infty^4)$ , and  $w^\lambda$  is their  $w_\infty$ . For the model currents presented in this study (bold lines),  $n^\lambda$  is the quantity  $(0.85n_\infty^2 + 0.15p_\infty)$ , and  $w^\lambda$  is the quantity  $(w_\infty^4)$ . Time constants  $\tau_n$  and  $\tau_w$  represent values at  $22^\circ C$ . Note, for  $I_{HT}$ , two  $I$ - $V$  relations are shown for the Perney and Kaczmarek bushy cell model. The first  $I$ - $V$  relation (1) corresponds to the current-clamp simulation in their Fig. 12D [ $\bar{g}_{HT} = 180$  nS, according to Kanemasa et al. (1995)]. The second  $I$ - $V$  relation (2) corresponds to the phaselocking simulation in their Fig. 14 ( $\bar{g}_{HT} = 50,000$  nS).

value computed from our population of isolated VCN cells (Rothman and Manis 2003a). Given a typical neuronal specific membrane capacitance of  $0.9 \mu\text{F}/\text{cm}^2$  (Gentet et al. 2000), the diameter of the soma model comes to  $\sim 21 \mu\text{m}$ , a value also in agreement with our isolated VCN cells (Rothman and Manis 2003a).

### Model sodium current

Due to the fast kinetics and large magnitude of  $I_{\text{Na}}$  in isolated VCN cells, we did not characterize this current, but instead looked to other voltage-clamp studies in mammalian neurons to derive its model. In particular, we used data from native TTX-sensitive  $\text{Na}^+$  currents at  $\sim 22^\circ\text{C}$ : (Belluzzi et al. 1985; Costa 1996; Ogata and Tatebayashi 1993; Parri and Crunelli 1998; Sah et al. 1988; Schild and Kunze 1997). Together, these studies provided sufficient data to compute steady-state activation/inactivation functions in the range  $-100$  to  $+40 \text{ mV}$  ( $m_\infty$  and  $h_\infty$ ), as well as activation/inactivation time constants ( $\tau_m$  and  $\tau_h$ ; see APPENDIX). Based on the studies of Costa (1996) and Belluzzi et al. (1985), model  $I_{\text{Na}}$  was given the following instantaneous current-voltage ( $I$ - $V$ ) relation

$$I_{\text{Na}} = \bar{g}_{\text{Na}} \cdot m^3 h \cdot (V - V_{\text{Na}}) \quad (2)$$

where  $\bar{g}_{\text{Na}}$  is the peak  $\text{Na}^+$  conductance, and  $V_{\text{Na}}$  the reversal potential of  $I_{\text{Na}}$  ( $+55 \text{ mV}$ ). Comparison of the model current traces as well as steady-state  $I$ - $V$  relations with the experimental data shows a close agreement. The activation threshold of model  $I_{\text{Na}}$  ( $V_{\text{th}} \cong -49 \text{ mV}$ ) is also in agreement with the activation thresholds of the  $\text{Na}^+$  current measured from our population of isolated VCN neurons (data not shown).

### Model hyperpolarization-activated cation current

Results from our previous study indicate the majority of VCN neurons possess a hyperpolarization-activated inward current (Rothman and Manis 2003a). Because this inward current activated with slow kinetics, we assumed it was similar to the mixed-cation current  $I_h$  rather than the near-instantaneously activating inward current  $I_{\text{KIR}}$  (Travagli and Gillis 1994). Evidence from experimental studies in the VCN supports this choice. First, the inward current measured in VCN neurons is resistant to blockade by barium (Bal and Oertel 2000; Schwarz and Puil 1997), suggesting it is a form of  $I_h$  rather than  $I_{\text{KIR}}$  (Travagli and Gillis 1994). Second, the current reverses positive to the resting membrane potential (Bal and Oertel 2000; Rusznak et al. 1996), consistent with a mixed-cation selective conductance rather than a  $\text{K}^+$ -selective conductance.

Like model  $I_{\text{Na}}$ , model  $I_h$  was derived from other voltage-clamp studies. Three of these studies pertained to auditory neurons (Banks et al. 1993; Fu et al. 1997; Rusznak et al. 1996), and two pertained to nonauditory neurons (Huguenard and McCormick 1992; Travagli and Gillis 1994). Based on these five studies, model  $I_h$  was given the following instantaneous  $I$ - $V$  relation

$$I_h = \bar{g}_h \cdot r \cdot (V - V_h) \quad (3)$$

where  $\bar{g}_h$  is the maximum steady-state conductance,  $V_h$  the reversal potential of  $I_h$  ( $-43 \text{ mV}$ ), and  $r$  the time and voltage-dependent activation variable with steady-state value  $r_\infty$  and time constant  $\tau_r$  (see APPENDIX). Here,  $\tau_r$  was predominantly based on the Huguenard and McCormick study (1992).

Subsequent to the specification of our model  $I_h$ , Bal and Oertel (2000) published a characterization of  $I_h$  in VCN octopus cells. The properties of  $I_h$  in octopus cells differs from our model values in that the activation curve sits  $10 \text{ mV}$  more depolarized, the rates of activation and deactivation are faster, and  $\bar{g}_h$  is larger than that used in this study. The faster rates probably reflect the higher experimental temperature in the Bal and Oertel study ( $33^\circ\text{C}$ ) in comparison to the Huguenard and McCormick study ( $23^\circ\text{C}$ ), and the large  $\bar{g}_h$  is probably

an unusual characteristic of octopus cells. We in fact explore the consequences of changing  $\bar{g}_h$  in this study as well as shifting the activation curve of  $I_h$  to more depolarized potentials. We also decrease the rate constant  $\tau_r$  by a Q10 factor of 3 when investigating the model at higher temperatures.

### Model leakage current

The leakage current was modeled as follows

$$I_{\text{lk}} = \bar{g}_{\text{lk}} \cdot (V - V_{\text{lk}}) \quad (4)$$

where  $\bar{g}_{\text{lk}}$  is the maximum steady-state conductance ( $2 \text{ nS}$ ), and  $V_{\text{lk}}$  the reversal potential of  $I_{\text{lk}}$  ( $-65 \text{ mV}$ ). Although it is common practice with HH-like models to adjust the resting membrane potential  $V_{\text{rest}}$  by adjusting  $V_{\text{lk}}$ , we fixed  $V_{\text{lk}}$  at  $-65 \text{ mV}$ . Fixing  $V_{\text{lk}}$  allows  $V_{\text{rest}}$  to vary in response to changes in other currents, such as  $I_{\text{LT}}$  and  $I_h$ . As will be shown in RESULTS, both  $I_{\text{LT}}$  and  $I_h$  can play an important role in setting  $V_{\text{rest}}$ .

### Model excitatory post-synaptic current

Excitatory post-synaptic currents (EPSCs) from auditory nerve (AN) fibers were modeled by the following equation

$$I_{\text{E}} = g_{\text{E}} \cdot (V - V_{\text{E}}) \quad (5)$$

where  $V_{\text{E}}$  is the reversal potential of  $I_{\text{E}}$  ( $0 \text{ mV}$ ), and  $g_{\text{E}}$  the time-dependent conductance change in response to an excitatory synaptic input. For simplicity,  $g_{\text{E}}$  was modeled as an  $\alpha$ -wave of the form

$$g_{\text{E}} = \bar{g}_{\text{E}}(t/\tau_{\text{E}}) \exp[1 - (t/\tau_{\text{E}})] \quad (6)$$

where  $\bar{g}_{\text{E}}$  determines the peak conductance and  $\tau_{\text{E}}$  the time to peak. For most of the simulations in this study,  $\tau_{\text{E}} = 0.4 \text{ ms}$ , resulting in an EPSC half width  $\sim 1 \text{ ms}$ , a  $10$ – $90\%$  rise time  $\sim 0.2 \text{ ms}$ , and a decay time  $\sim 0.6 \text{ ms}$  at  $22^\circ\text{C}$ . These values are comparable to those of fast non-NMDA receptor-mediated EPSCs recorded from auditory-pathway neurons at  $22^\circ\text{C}$  (Barnes-Davies and Forsythe 1995; Isaacson and Walmsley 1995; Zhang and Trussell 1994). Example waveforms of  $g_{\text{E}}$  can be found in Fig. 6. To simulate the effects of converging AN input, the model includes up to 50 independent  $I_{\text{E}}$ 's in parallel.

### Model parameters and properties

Table 1 lists the parameter settings for the five different model configurations investigated in this study: the Type I-c, Type I-t, Type I-II, Type II-I, and Type II model. These canonical configurations were derived from the four cell types previously described (Rothman and Manis 2003a), where the Type I-c cells were those cells that,

TABLE 1. Model parameters and properties

	Model Type				
	I-c	I-t	I-II	II-I	II
$\bar{g}_{\text{Na}}$ , nS	1000	1000	1000	1000	1000
$\bar{g}_{\text{HT}}$ , nS	150	80	150	150	150
$\bar{g}_{\text{LT}}$ , nS	0	0	20	35	200
$\bar{g}_{\text{A}}$ , nS	0	65	0	0	0
$\bar{g}_h$ , nS	0.5	0.5	2	3.5	20
$\bar{g}_{\text{lk}}$ , nS	2	2	2	2	2
$V_{\text{rest}}$ , mV	-63.9	-64.2	-64.1	-63.8	-63.6
$R_{\text{rest}}$ , M $\Omega$	473	453	312	244	71
$\tau_m$ , ms	7.0	4.0	3.7	2.9	0.9
$V_{\text{th}}$ , mV	-38.3	-34.9	-51.2	-58.0	-62.2
$S_{-50/-70}$ , nS	0.3	0.3	5.0	12.6	49.5
$\bar{g}_{\text{E}\theta}$ @ $22^\circ\text{C}$ , nS	2.0	2.2	2.8	3.2	8.6
$\bar{g}_{\text{E}\theta}$ @ $38^\circ\text{C}$ , nS	11	12	15	17	34



under voltage clamp, displayed only  $I_{HT}$ , the Type I-t cells displayed both  $I_{HT}$  and  $I_A$ , and the Type II cells displayed both  $I_{HT}$  and  $I_{LT}$ . The two intermediate model types (Type I-II and Type II-I) refer to the intermediate experimental Type I-i cell. As in the experimental data, both intermediate types fall between Type I and Type II, due to the presence of small  $I_{LT}$ ; however, the Type I-II model is closer to being Type I, and the Type II-I model is closer to being Type II. Listed below each model type in Table 1 are the conductance values used in its simulation. Values for  $\bar{g}_A$ ,  $\bar{g}_{LT}$ , and  $\bar{g}_{HT}$  were based on experimental data (Rothman and Manis 2003a). For simplicity and ease of comparison between model responses, single values of  $\bar{g}_{Na}$  and  $\bar{g}_{K}$  were chosen: 1,000 and 2 nS, respectively. The value of  $\bar{g}_{Na}$  was chosen to give large, reliable APs in all five model types, and the value of  $\bar{g}_{K}$  was chosen to give the Type I-c model a realistic input resistance (see following text). The value of  $\bar{g}_h$ , on the other hand, was not kept the same for all model simulations but instead was adjusted to keep  $V_{rest}$  near  $-64$  mV. Note that we used  $I_h$  as a means of setting  $V_{rest}$  instead of  $I_{K}$  since modulation of  $I_h$  could be a mechanism for setting  $V_{rest}$ , especially in Type II cells. For simulations where  $\bar{g}_{LT} > 0$  (i.e. the Type II, Type I-II and Type II-I simulations),  $\bar{g}_h$  was one-tenth that of  $\bar{g}_{LT}$ . For the Type I-c and Type I-t model,  $\bar{g}_h$  was set to a small value of 0.5 nS because larger values produced hyperexcitability. The value of  $\bar{g}_h$  in the Type II model (20 nS) is similar to values reported in medial nucleus of the trapezoid body (MNTB) neurons (Banks et al. 1993). MNTB neurons share many physiological and anatomical features with VCN bushy cells (i.e. Type II cells), including the presence of strong inward rectification at hyperpolarized potentials. However, this value of  $\bar{g}_h$  is lower than that estimated for VCN octopus cells (Bal and Oertel 2000).

Table 1 also lists seven parameters computed from each model type that are consistent with the experimental data. The parameters are as follows.

1) The resting membrane potential,  $V_{rest}$ . For all models,  $V_{rest} \cong -64$  mV, a value consistent with VCN neurons (Oertel 1983). For the Type I-c and Type I-t models,  $V_{rest}$  is primarily determined by  $I_{K}$  because this current is the largest at rest. For the Type I-II, Type II-I, and Type II models, however,  $V_{rest}$  is primarily determined by  $I_h$  and  $I_{LT}$  because these currents are largest at rest. In fact, removal of  $I_{K}$  from these models produces little change in  $V_{rest}$ . Hence it is possible to model the latter three models without  $I_{K}$ .

2) The resting membrane resistance,  $R_{rest}$ , computed by taking the reciprocal of the sum of all conductances at  $V_{rest}$ . As Table 1 shows, the Type I-t and Type I-c models show the largest  $R_{rest}$ , which equals  $\sim 1/\bar{g}_{K}$ . The other three models (Type I-II, Type II-I, and Type II) show decreasing values of  $R_{rest}$ , consistent with a parallel increase in  $\bar{g}_h$  and  $\bar{g}_{LT}$ . That  $R_{rest}$  is larger in the Type I-c and Type I-t models than in the Type II model is consistent with previous experimental findings that  $R_{rest}$  is significantly larger in VCN Type I cells [ $447 \pm 265$  (SD) M $\Omega$ ] than in Type II cells [ $225 \pm 160$  M $\Omega$ ] (Manis and Marx 1991).

3) The resting membrane time constant,  $\tau_{rest}$ , computed by multiplying  $R_{rest}$  by  $C_m$ . Again,  $\tau_{rest}$  is larger in the Type I-c and Type I-t models than in the Type II model, consistent with previous experimental findings that  $\tau_{rest}$  is significantly larger in Type I cells ( $6.5 \pm 7$  ms) than in Type II cells ( $1.69 \pm 0.63$  ms) (Manis and Marx 1991).

4)  $V_{th}$  and  $S_{-50/-70}$  values, computed from model voltage-clamp simulations (i.e. steady-state  $I$ - $V$  relations), where  $V_{th}$  is the voltage at which the whole cell steady-state current reaches a value of 0.1 nA, and  $S_{-50/-70}$  is the slope of a steady-state  $I$ - $V$  relation from  $-50$  to  $-70$  mV. To simulate the same experimental conditions of our isolated VCN data, that is, to simulate the block of  $I_{Na}$  with TTX and to simulate off-line linear leak subtraction,  $\bar{g}_{Na} = 0$  and  $\bar{g}_{K} = 0$  in these voltage-clamp simulations. Comparison of the model values with the experimental data (see Fig. 4) again shows the model closely agrees with the experimental data.

5) The last parameter,  $\bar{g}_{E\theta}$ , denotes synaptic efficacy or strength of an individual AN synapse. Specifically,  $\bar{g}_{E\theta}$  is defined as the smallest

value of  $\bar{g}_E$  (Eq. 6) necessary for a single AN synapse to generate an AP. A comparison across model types in Table 1 shows that  $\bar{g}_{E\theta}$  is larger in the Type II model than in the Type I-c and Type I-t models. This disparity of  $\bar{g}_{E\theta}$  values is due to the magnitude difference of  $I_{LT}$ :  $I_{LT}$ , being a  $K^+$  current with significant activation near rest, acts to oppose synaptic depolarization.

### Definition of sub- and suprathreshold synaptic inputs

The fact that a given value of  $\bar{g}_E$  may be suprathreshold in the Type I-c model but subthreshold in the Type II model poses a problem when trying to compare model responses to what one would like to be the "same" AN input. To resolve this problem, we normalized values of  $\bar{g}_E$  with respect to  $\bar{g}_{E\theta}$ , such that for all *subthreshold inputs*,  $\bar{g}_E = 0.5\bar{g}_{E\theta}$ , and for all *suprathreshold inputs*,  $\bar{g}_E = 3\bar{g}_{E\theta}$ . In this way, AN synapses share the same synaptic efficacy rather than the same peak conductance.

## RESULTS

We present our results in four sections. In the first section, we examine current-clamp responses of each model type and compare them to responses of real VCN neurons. In the second section, we compare model EPSPs resulting from the same effective synaptic input and explore the effects of subthreshold currents, such as  $I_{LT}$  and  $I_h$ , on the shape of these EPSPs. In the third section, we explore the effects of each  $K^+$  current on AP shape as well as the rate of repetitive firing in the Type I models. In the last section, we explore the responses to simulated trains of convergent AN inputs with respect to phase locking, PSTHs, and regularity analysis, again comparing results to those of real VCN neurons.

### Model current-clamp responses

MODEL CURRENT-CLAMP RESPONSES RESEMBLE THOSE OF REAL VCN NEURONS. Because VCN neurons are typically classified by their response to current injection as either Type I or Type II (Manis and Marx 1991; Wu and Oertel 1984), it was of particular interest to investigate the behavior of the VCN model under current-clamp conditions. Hence, each model listed in Table 1 was investigated with respect to hyperpolarizing and depolarizing current steps, similar in magnitude to those used *in vitro*. Results are summarized in Fig. 2, where model responses to a depolarizing (+) and hyperpolarizing (−) current pulse are plotted concurrently. In *A* and *B*, the response of the Type I-c and Type I-t model to small current injection is clearly Type I, responding to a small depolarizing current pulse (+50 pA) with a train of regularly spaced APs and responding to a small hyperpolarizing current pulse (−50 pA) with an exponential decay of the membrane potential. These models are nearly indistinguishable except that the Type I-t model shows a higher discharge rate than the Type I-c model during the same current step. VCN neurons with such a "Type I" response have been morphologically identified as stellate cells (Wu and Oertel 1984).

In Fig. 2C, the response of the Type II model to large current injection is clearly Type II, responding to a large depolarizing current pulse (+300 pA) with a single AP followed by a steady depolarization and responding to a large hyperpolarizing current pulse (−300 pA) with a non-exponential decay of the membrane potential, followed by a "sag" back to  $V_{rest}$  (i.e. inward rectification). At the termination of the hyperpolarizing

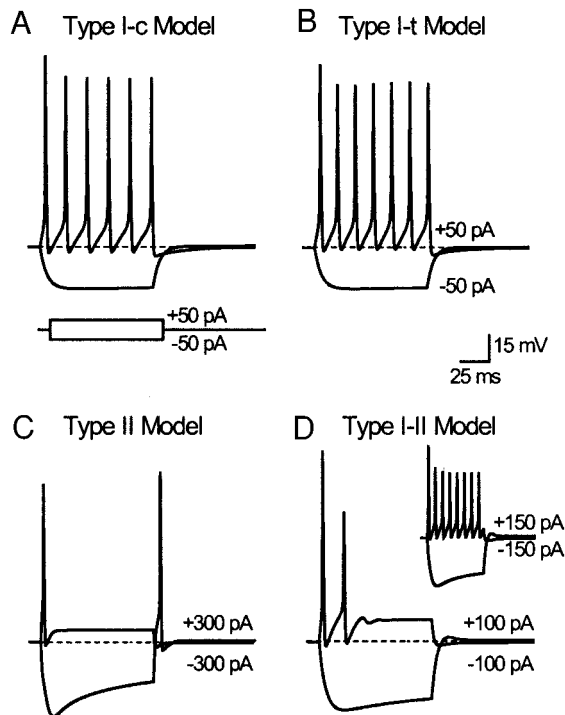


FIG. 2. Current-clamp responses of the Type I-c (A), Type I-t (B), Type II (C), and Type I-II model (D), for positive and negative current injection ( $\pm I_{\text{ext}}$ ). Example current pulses are shown in A. Inset: an extra simulation with larger  $I_{\text{ext}}$ , demonstrating the Type I-II model can display a regular discharge of action potentials (APs) similar to the Type I-c model. Conductance values for these simulations are given in Table 1. Scale bars for all voltage traces. Dashed lines denote  $V_{\text{rest}}$  (approximately  $-64$  mV).  $T = 22^\circ\text{C}$ .

pulse, the Type II model displays an anodal-break spike, yet another classic sign of the Type II response. VCN neurons with such a Type II response have been morphologically identified as bushy cells (Wu and Oertel 1984).

In Fig. 2D, the response of the Type I-II model is intermediate in that it displays one or two APs in response to a small depolarizing current pulse ( $+100$  pA) but a regular discharge of APs in response to a larger depolarizing current pulse ( $+150$  pA). Similarly, the Type II-I model displays one or two APs in response to a small depolarizing current pulse. However, in response to a larger depolarizing current pulse, the Type II-I model displays only three or four APs rather than a regular train of APs (see Fig. 4). VCN neurons with such intermediate current-clamp responses have in fact been observed in several studies (Francis and Manis 2000; Manis and Marx 1991; Oertel 1991; Schwarz and Puil 1997).

$I_{\text{LT}}$  IS RESPONSIBLE FOR THE CLASSIC TYPE II CURRENT-CLAMP RESPONSE. The Type I-c and Type II models differ only in the magnitudes of  $I_{\text{LT}}$  and  $I_{\text{h}}$  (see Table 1). To determine the relative roles these currents play in producing the Type II current-clamp response, the Type II model was simulated with either  $I_{\text{LT}} = 0$  or  $I_{\text{h}} = 0$ . When  $I_{\text{h}} = 0$ , the model no longer displayed inward rectification during a hyperpolarizing current pulse but still displayed the characteristic Type II response of a single AP at the onset of a depolarizing current pulse (Fig. 3B). When  $I_{\text{LT}} = 0$ , on the other hand, the model displayed a regular discharge of APs in response to a depolarizing current pulse (Fig. 3D), similar to the canonical Type I current-clamp response in Fig. 2A. Hence,  $I_{\text{LT}}$  is responsible for the phasic

discharge pattern of the Type II model. These results coincide with those of Brew and Forsythe (1995) and Rathouz and Trussell (1998), who found that auditory neurons that normally display a single AP in response to a depolarizing current pulse (rat MNTB neurons and avian n. magnocellularis neurons, respectively) displayed a regular discharge of APs in response to a depolarizing current pulse after blocking  $I_{\text{LT}}$  with dendrotoxin.

Figure 3 reveals three other notable results. First, when  $I_{\text{HT}} = 0$  (C), the only change in the model is a slight change in AP shape, which is not evident in this figure. Second,  $V_{\text{rest}}$  shifts negative when  $I_{\text{h}} = 0$  (B), and shifts positive when  $I_{\text{LT}} = 0$  (D). The shifts arise because  $V_{\text{rest}}$  is not constrained but varies according to the sum of the membrane currents (these shifts are explained further in the following text). It could be argued that the shifts in  $V_{\text{rest}}$  are the source of change in the model's current-clamp response; however, when  $V_{\text{rest}}$  is held constant across conditions via a steady holding current, the same conclusions about  $I_{\text{LT}}$  are drawn (not shown). Finally, the model does not show an anodal-break spike when  $I_{\text{h}} = 0$ , suggesting  $I_{\text{h}}$  plays an influential role in generating anodal-break spikes. The influence of  $I_{\text{h}}$  is even more apparent when  $I_{\text{LT}} = 0$ , in which case the model now responds with a train of APs at the end of a hyperpolarizing current pulse, lasting  $\sim 400$  ms (D). When the depolarizing effects of  $I_{\text{h}}$  are counteracted with a holding current of  $-50$  pA, this train of APs disappears (not shown).

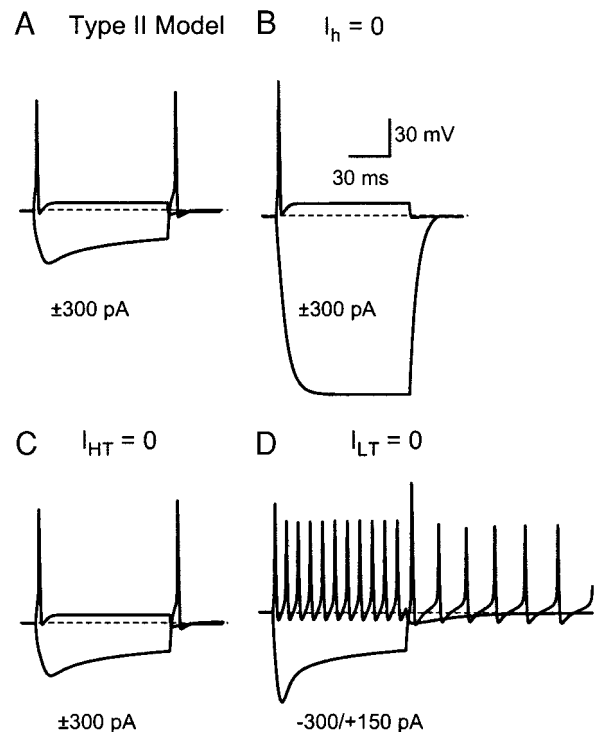


FIG. 3.  $I_{\text{LT}}$  is responsible for the Type II current-clamp response. A: Type II model when  $I_{\text{ext}} = \pm 300$  pA. B: same as A, except  $I_{\text{h}} = 0$ . The model's response to  $+I_{\text{ext}}$  is still Type II. The response to  $-I_{\text{ext}}$  no longer shows inward rectification, and there is no anodal-break spike. C: same as A, except  $I_{\text{HT}} = 0$ . The response is still Type II. D: same as A, except  $I_{\text{LT}} = 0$ . The response to  $+I_{\text{ext}}$  is now Type I. Here,  $I_{\text{ext}} = 150$  pA because larger steps caused a steady depolarization that prevented AP generation. Note the long train of APs at the end of  $-I_{\text{ext}}$ , due to a more depolarized  $V_{\text{rest}}$ . Scale bars for all voltage traces. ---,  $V_{\text{rest}}$ .  $T = 22^\circ\text{C}$ .

VARIATION OF  $I_{LT}$  LEADS TO A VARIATION OF CURRENT-CLAMP RESPONSES. The preceding results demonstrate  $I_{LT}$  is the main current responsible for producing the Type II current-clamp response in the Type II model. However, results from the other simulations (Type I-II and Type II-I) with lower amounts of  $I_{LT}$  demonstrate that the simple presence of  $I_{LT}$  is not enough to create a Type II current-clamp response, but rather a certain level of  $I_{LT}$  is necessary. This is demonstrated in Fig. 4, which shows the model's current-clamp response as a function of  $\bar{g}_{LT}$ . As this figure shows, changing  $\bar{g}_{LT}$  over the physiologically measured range 0–600 nS significantly affects the model's current-clamp response. When  $\bar{g}_{LT} < 20$  nS, the model fires regularly, regardless of the injected current. When  $\bar{g}_{LT} > 35$  nS, the model fires one or two action potentials, regardless of the injected current. When  $\bar{g}_{LT}$  is the range 20–35 nS, however, the model shows intermediate behavior that is level dependent: single APs are produced in response to small depolarizing currents, but two or more APs in response to larger depolarizing currents.

Because it was also of interest to relate these findings to the results presented in our previous study (Rothman and Manis 2003a),  $V_{th}$  and  $S_{-50/-70}$  values were computed from the model's  $I$ - $V$  relation. As Fig. 4 shows, a variation of  $\bar{g}_{LT}$  produces a range of  $V_{th}$  and  $S_{-50/-70}$  values ( $\Delta$ ): from  $\bar{g}_{LT} = 0$  ( $V_{th} = -38.2$  mV,  $S_{-50/-70} = 0.3$  nS), to  $\bar{g}_{LT} = 600$  nS ( $V_{th} = -63$  mV,  $S_{-50/-70} = 147.7$  nS). Remarkably, the trajectory of model simulations as  $\bar{g}_{LT}$  increases follows the same trajectory of the experimental data ( $\blacktriangle$ ) (from Rothman and Manis 2003a, Fig. 7). These results lend strong support to the hypothesis that a gradient of  $I_{LT}$  is responsible for the large dispersion of  $V_{th}$  and  $S_{-50/-70}$  values observed experimentally. In addition, the same threshold and slope analyses was computed for simulations in which  $I_{LT} = 0$ , and the magnitude of  $I_{HT}$  varied ( $\bar{g}_{HT} = 50$ –600 nS, where 600 nS is well above the highest value measured from the isolated VCN cells). Under these conditions,  $V_{th}$  only spanned from  $-44$  to  $-32$  mV, and  $S_{-50/-70}$  remained near zero. Hence, a variation of  $I_{HT}$  cannot account for the dispersion of  $V_{th}$  and  $S_{-50/-70}$  values observed in the experimental data.

TYPE II MODEL EXHIBITS STRONG OUTWARD AND INWARD RECTIFICATION.  $I$ - $V$  relations of the models listed in Table 1 were computed from their steady-state current-clamp responses, similar to those in Fig. 2 ( $I_{Na} = 0$  to inhibit AP generation). As the results in Fig. 5 show, all model types exhibit outward rectification at  $V > V_{rest}$ , due to their outward currents. However, outward rectification in the Type I-c and Type I-t models occurs at higher potentials ( $V > -45$  mV, where  $I_{HT}$  begins to activate) in comparison to the Type II and intermediate models ( $V > V_{rest}$ , where  $I_{LT}$  begins to activate). The difference in outward rectification is a clear demonstration of how increasing levels of  $I_{LT}$  cause increasing amounts of outward rectification. Figure 5 also shows that, at  $V < V_{rest}$ , all model types exhibit inward rectification, due to  $I_h$ . Hence, increasing levels of  $I_h$  cause increasing amounts of inward rectification, as denoted in Fig. 5.

The difference in slope between the Type I-c and Type II model  $I$ - $V$  relations is dramatic: whereas the Type I-c  $I$ - $V$  relation is steep from  $-100$  to  $-50$  mV, the Type II  $I$ - $V$  relation is relatively flat. As just mentioned, these differences are due to  $I_{LT}$  and  $I_h$ , which tend to flatten out, or rectify the model's  $I$ - $V$  relation above and below  $V_{rest}$ . The input resistance at  $V_{rest}$  shows a sevenfold difference between models (Table 1,  $R_{rest}$ ). The sevenfold difference in input resistance in turn reflects a sevenfold difference in the resting membrane time constant because both models share the same membrane capacitance ( $\tau_m = R_{rest}C_m$  at rest).

#### Model EPSPs

In this section, the effects of the different currents on EPSP integration are examined. For simplicity, only results from the Type II and Type I-c models are presented because these models represent the extreme cases of having and not having  $I_{LT}$ . It should be noted, however, that as before, results of the Type I-t model are similar to those of the Type I-c model, and results from the intermediate models fall between those of the Type I-c and Type II models.

WHEREAS THE TYPE I-C MODEL ACTS AS AN EPSP INTEGRATOR, THE TYPE II MODEL ACTS AS AN EPSP COINCIDENCE DETECTOR. Figure 6A shows that the half-width of the EPSP elicited by a

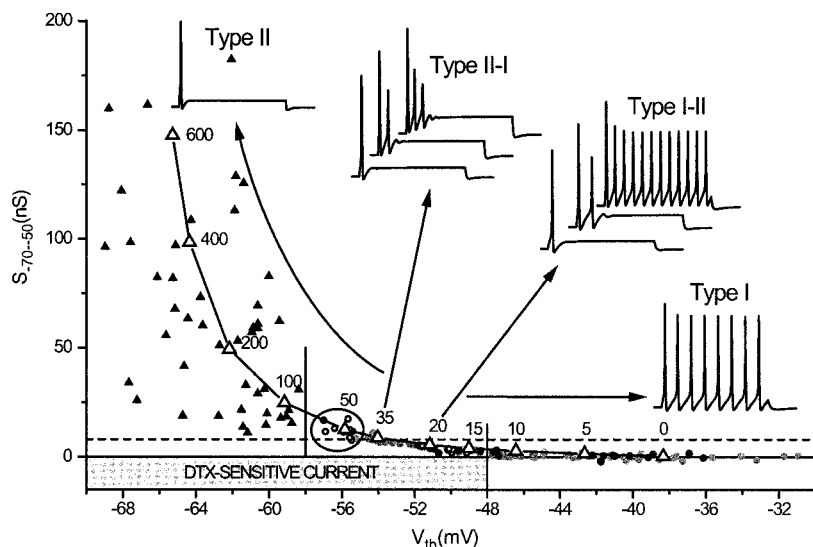


FIG. 4. Variation of  $I_{LT}$  produces a variation of model responses. Results of 11 Type I-c simulations with increasing  $\bar{g}_{LT}$  (0–600 nS).  $\Delta$ ,  $V_{th}$  and  $S_{-50/-70}$  values computed from steady-state  $I$ - $V$  relations. Above each  $\Delta$  is the value of  $\bar{g}_{LT}$ . Hence, as  $\bar{g}_{LT}$  increases,  $V_{th}$  shifts negative and  $S_{-50/-70}$  positive, following the trajectory of real VCN neurons ( $\blacktriangle$ ) (data from Rothman and Manis 2003a, Fig. 7). For  $\bar{g}_{LT} < 20$  nS, model responses are Type I, for  $\bar{g}_{LT} > 35$  nS, model responses are Type II, and for  $20 \leq \bar{g}_{LT} \leq 35$  nS, model responses are intermediate, displaying a single AP in response to a small current pulse and multiple APs in response to a larger current pulse. Whereas at the highest current pulse, the intermediate Type II-I model ( $\bar{g}_{LT} = 35$  nS) displays 3 APs, the intermediate Type I-II model ( $\bar{g}_{LT} = 20$  nS) displays repetitive firing.  $T = 22^\circ\text{C}$ .



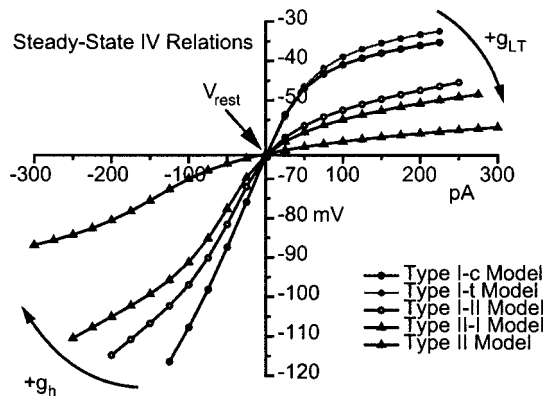


FIG. 5. Steady-state  $I$ - $V$  relations of the 5 models listed in Table 1, computed from current-clamp simulations similar to those in Fig. 2, except  $I_{Na} = 0$ .  $T = 22^\circ\text{C}$ .

synaptic current with  $\bar{g}_E = 1$  nS is significantly briefer in the Type II model (1.6 ms) than in the Type I-c model (7.1 ms). Inspection of the EPSPs reveals faster EPSP rise and decay times in the Type II model. These differences in EPSP shape are due to a smaller  $\tau_m$  in the Type II model, as described in the preceding text.

One consequence of the long-duration EPSP in the Type I-c model and a very brief EPSP in the Type II model is that the Type I-c model operates as an EPSP integrator, whereas the Type II model operates as an EPSP coincidence detector. This is demonstrated in Fig. 6B, which shows model responses to pairs of subthreshold synaptic inputs of equal amplitude, separated in time. When the interval between the two EPSPs is short, both models show EPSP summation (EPSPs that rise above  $-\infty$ ). However, EPSP summation occurs over significantly longer intervals in the Type I-c model ( $\sim 40$  ms) than in the Type II model ( $\sim 2$  ms). Hence, the Type I-c model temporally integrates its synaptic input, whereas the Type II model acts as a synaptic coincidence detector. Interestingly, an afterhyperpolarization (AHP) follows each EPSP in the Type II model (Fig. 6A,  $\blacktriangle$ ) due to activation of  $I_{LT}$ . As Fig. 6B shows, inputs that arrive during this AHP are smaller than the primary EPSP ( $\blacktriangle$ ), thus enhancing coincidence detection in the Type II model.

Figure 6C shows the Type I-c model response to a train of subthreshold synaptic inputs arriving at 333 Hz (top). Here, consecutive EPSPs sum together to cause a depolarization that eventually leads to the generation of APs. When this simulation is carried out for a longer time, the model displays repetitive firing reminiscent of the current-clamp response in Fig. 2A. Moreover, repeating the same analysis at two different frequencies demonstrates that the rate of firing is directly proportional to the rate of incoming EPSPs (17 spikes/s at 250 Hz, 25 spikes/s at 333 Hz, 67 spikes/s at 1,000 Hz). Hence the Type I-c model is well suited to measure the average rate, or intensity, of its synaptic input. This contrasts to the Type II model, where subthreshold synaptic inputs do not sum together in time, and therefore do not generate output spikes (Fig. 6C, middle).

$I_{LT}$  AND  $I_h$  HAVE DISTINCT EFFECTS ON THE TYPE II MODEL EPSP. Although both  $I_h$  and  $I_{LT}$  act to reduce  $\tau_m$  near  $V_{rest}$ , their effect on the Type II model's EPSP is quite distinct. This is apparent when the effect of each conductance is studied independently; i.e., setting both  $I_h$  and  $I_{LT}$  to zero in the Type

II model and then adding them back one at a time. Such an analysis is shown in Fig. 7A, where the EPSP of the reduced Type II model is plotted on the left ( $-I_{LT} - I_h$ ). As Fig. 7A shows, adding  $I_h$  to the reduced model has two effects: a small decrease in EPSP width and a depolarization of  $V_{rest}$  ( $-I_{LT} + I_h$ ). In contrast, adding  $I_{LT}$  to the reduced model produces a dramatic decrease in EPSP width and a hyperpolarization of  $V_{rest}$  ( $+I_{LT} - I_h$ ). Here the reductions in EPSP width are due to a decrease in the model's input resistance, which leads to a concomitant decrease in  $\tau_m$ . The shifts in  $V_{rest}$  are due to the fact that both  $I_h$  and  $I_{LT}$  act to move  $V_{rest}$  toward their respective reversal potential ( $-43$  and  $-70$  mV). From this analysis, we see that if the goal is to have the briefest EPSP possible (that of approximating an ideal EPSP coincidence detector), then  $I_h$  alone is an inefficient means of doing so: not only is  $I_h$ 's effect on the EPSP width small, but it depolarizes  $V_{rest}$  toward the threshold of AP generation, producing a hyperexcitable model (see Fig. 3D). Using  $I_{LT}$  alone, on the other hand, is an efficient means of reducing the model's EPSP width without inducing hyperexcitability. And yet, the scenario with  $I_{LT}$  alone is suboptimal because  $I_{LT}$  hyperpolarizes  $V_{rest}$  toward  $V_K$ , in which case  $<2\%$  of  $I_{LT}$  is activated. To produce the briefest EPSP possible, it is necessary to have a larger fraction

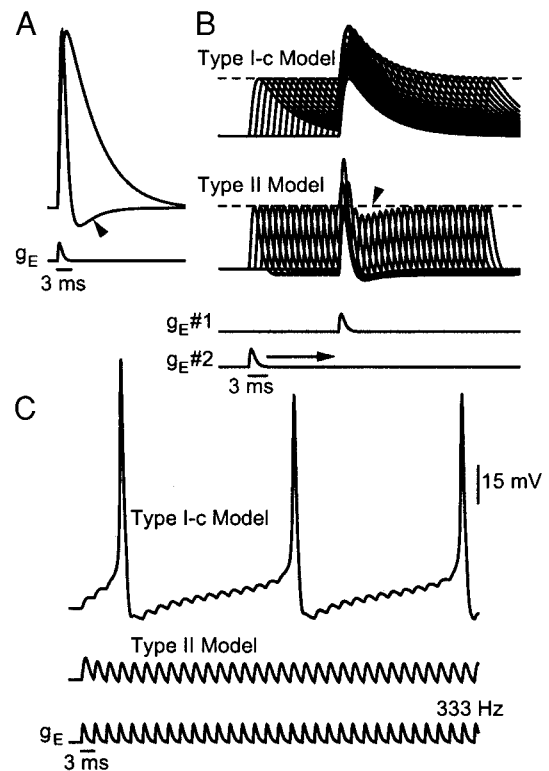


FIG. 6. Model excitatory postsynaptic potentials (EPSPs). A: comparison of EPSPs of the Type I-c model (slow decay) to the Type II model (fast decay), elicited by the same auditory nerve (AN) input at bottom ( $\bar{g}_E = 1$  nS). EPSPs were normalized for comparison.  $\blacktriangle$ , an afterhyperpolarization (AHP) that follows the Type II EPSP. Time scale bar (3 ms) appears below  $\bar{g}_E$ . B: model responses to 2 subthreshold AN inputs with equal amplitude ( $\bar{g}_E = 0.5\bar{g}_{E0}$ ) but different arrival times:  $t_1 = 15$  ms,  $t_2 = 0$ –40 ms. For the Type I-c model, EPSPs summed over an extended period of time ( $t_2 = 0$ –40 ms). For the Type II model, synaptic inputs summed over a brief period of time ( $t_2 = 19$ –21 ms).  $---$ , height of an isolated EPSP.  $\blacktriangle$ , a depression of EPSP size in the Type II model. EPSPs normalized for comparison. C: response of the Type I-c (top) and Type II model (middle) to a train of subthreshold AN inputs of equal amplitude ( $\bar{g}_E = 0.5\bar{g}_{E0}$ ) arriving at 333 Hz.  $T = 22^\circ\text{C}$ .

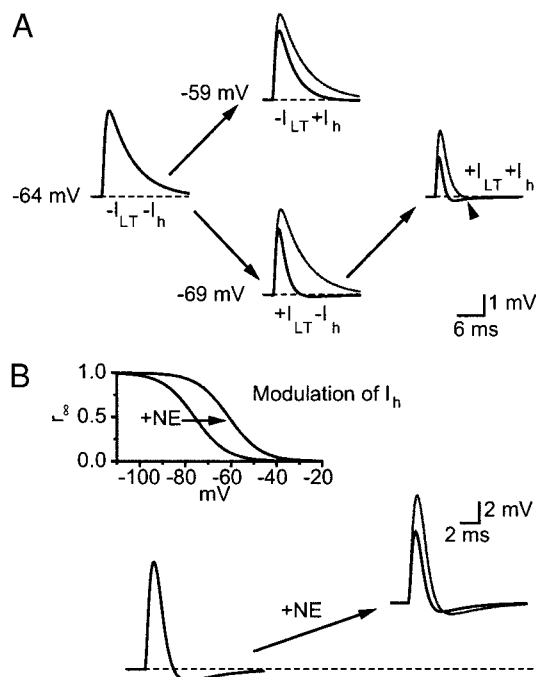


FIG. 7. Both  $I_{LT}$  and  $I_h$  shape the Type II model's EPSP. A: Type II model with (+) and without (−)  $I_{LT}$  and  $I_h$ . Arrowhead, an AHP appearing after addition of  $I_{LT}$ . For comparison, traces before the arrows are shown as gray traces after the arrows ( $V_{rest}$  adjusted appropriately). All EPSPs generated by the same AN input ( $\bar{g}_E = 1$  nS). B: simulation of a 15-mV shift in half-activation ( $V_{0.5}$ ) of  $I_h$  induced by a 20  $\mu$ M dose of norepinephrine (NE), as reported by Banks et al. (1993). Bottom: Type II model EPSPs before (left black trace, right gray trace;  $V_{0.5} = -76$  mV) and after (right black trace;  $V_{0.5} = -61$  mV) the shift. Dashed line,  $V_{rest}$  before the shift.  $T = 22^\circ\text{C}$ .

of  $I_{LT}$  activated because this would produce an even briefer EPSP. Hence with these observations in mind, one can see how a combination of  $I_h$  and  $I_{LT}$  act to produce a very brief EPSP, more so than with each conductance alone: 1)  $I_{LT}$  acts to decrease the EPSP width by reducing  $\tau_m$ , while 2)  $I_h$  counteracts the hyperpolarizing effects of  $I_{LT}$ , thereby maintaining  $V_{rest}$  at potentials where a significant amount of  $I_{LT}$  is activated. This is also demonstrated in Fig. 7A, where the addition of  $I_h$  to the reduced model with  $I_{LT}$  alone ( $+I_{LT} - I_h$ ) depolarizes  $V_{rest}$  back to  $-64$  mV, thereby raising the activation level of  $I_{LT}$  to  $\sim 6\%$ , thereby reducing the EPSP width even further ( $+I_{LT} + I_h$ ). Interestingly, after  $I_{LT}$  and  $I_h$  are reinstated to the Type II model, an AHP appears at the end of the EPSP (arrowhead). The AHP is a consequence of  $I_{LT}$  equilibrating back to its steady-state value at rest, and this effect is more pronounced when  $V_{rest}$  is further away from  $V_K$  ( $+I_{LT} + I_h$ ) than near  $V_K$  ( $+I_{LT} - I_h$ ).

Another effect of  $I_{LT}$  and  $I_h$  on the Type II model EPSP is a reduction in amplitude, as is clear in Fig. 7A ( $+I_{LT} + I_h$ ). This result too has implications for coincidence detection in that, with smaller EPSPs, it takes a larger number of coincident inputs to drive the membrane potential towards the threshold of AP generation, in which case the requirements for coincidence detection are even more stringent.

**MODULATION OF  $I_h$  MODULATES THE TYPE II MODEL EPSP WIDTH AND AMPLITUDE.** It has previously been reported that the activation curve of  $I_h$  can shift as much as 15–20 mV positive in the presence of either norepinephrine (NE) or the

membrane permeable analogue of cyclic-AMP, 8-Br-cAMP (Banks et al. 1993; Cuttle et al. 2001). This modulation of  $I_h$  could play an important role in increasing temporal acuity of VCN neurons by decreasing the width and amplitude of their EPSPs, thereby enhancing coincidence detection. We tested this hypothesis in the Type II model by shifting the steady-state activation curve of  $I_h$  ( $r_\infty$ ) 15 mV positive. Results are shown in Fig. 7B, where model EPSPs are shown before and after the shift in  $r_\infty$ . Comparison of EPSPs shows both a reduction in width and amplitude. The explanation of these results follows the same reasoning as in Fig. 7A: the shift in activation of  $I_h$  caused  $V_{rest}$  to depolarize, increasing the activation level of  $I_{LT}$ , thereby reducing the EPSP width and amplitude. The end result is a more ideal coincidence detector, as we demonstrate in *Model responses to AN-like inputs*.

### Model action potentials

**$I_{LT}$  AND  $I_h$  REDUCE THE MODEL REFRACTORY PERIOD.** Besides producing a brief EPSP, another consequence of a small  $\tau_m$  in the Type II model is a brief AHP following an AP, one that is significantly briefer than that of the Type I-c model (Fig. 8A). Fitting single exponential functions to the AHP time course reveals a twofold difference in time constants between the Type II and Type I-c model ( $\sim 6$  and 13 ms).

The shorter AHP in the Type II model coincides with a shorter refractory period (RP), as demonstrated in Fig. 8, B–D. In each panel of Fig. 8 are 30 Type II model responses to two

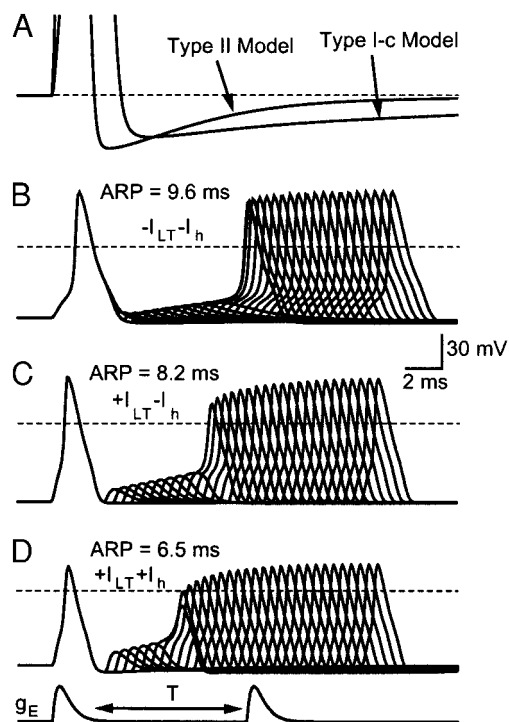


FIG. 8. AHP and refractory analysis. A: AHPs following an AP (truncated at left) in the Type I-c and Type II model. The Type II model returns to  $V_{rest}$  (---) faster than the Type I-c model. B: refractory analyses of the Type II model when  $I_{LT} = 0$  and  $I_h = 0$ . Responses are to 2 consecutive suprathreshold AN inputs with equal amplitude ( $\bar{g}_E = 3\bar{g}_{E0}$ ) but different inter-arrival times ( $T = 3-18$  ms). ---, AP trigger detection level. Absolute refractory period (ARP) defined as the smallest  $T$  generating 2 consecutive APs. C: same as B, except  $\bar{g}_{LT} = 200$  nS. D: same as B, except  $\bar{g}_{LT} = 200$  nS and  $\bar{g}_h = 20$  nS. Time scale bar for A–D. Voltage scale bar for B–D.  $T = 22^\circ\text{C}$ .



suprathreshold synaptic inputs of equal amplitude ( $\bar{g}_E = 3\bar{g}_{E0}$ ) separated by various intervals. When both  $I_h$  and  $I_{LT}$  are set to zero, the model displays a long RP ( $B$ , 9.6 ms), similar to the Type I-c model. When  $I_{LT}$  is reinstated to the model, the RP is reduced ( $C$ , 8.2 ms) but not as significantly as when both  $I_{LT}$  and  $I_h$  are reinstated together ( $D$ , 6.5 ms). Note although the shifts in  $V_{rest}$  are not obvious in this figure, the same voltage shifts occur as those in Fig. 7A.

Because the Type II model has a shorter RP than the Type I-c model, it follows a train of suprathreshold inputs better than the Type I-c model. This is demonstrated in Fig. 9, where the Type II model ( $B$ ) follows a suprathreshold AN input at 140 Hz better than the Type I-c model ( $A$ ). The ability to follow a synaptic input one-to-one can be quantified by an entrainment index, which is simply the ratio of output spikes to synaptic input events. Hence at 140 Hz, the entrainment index is 0.5 for the Type I-c model and 1.0 for the Type II model. Computing entrainment indexes over a range of frequencies (100–250 Hz) shows that the Type II model is consistently better than the Type I-c model at following a suprathreshold synaptic input one-to-one (Fig. 9C).

$I_{HT}$  SERVES TO REPOLARIZE THE MEMBRANE DURING AN AP. In the Type I-c model, the only  $K^+$  current besides  $I_{K1}$  is  $I_{HT}$ ; hence, it is primarily responsible for repolarizing the membrane during an AP. As Fig. 10A shows, modulation of  $I_{HT}$  produces a dramatic change in the rate of repolarization during the downstroke of the AP. When  $I_{HT}$  was set to very small values ( $\bar{g}_{HT} < 15$  nS), the membrane failed to repolarize back to  $V_{rest}$ . In the Type I-t model, there are two  $K^+$  currents that

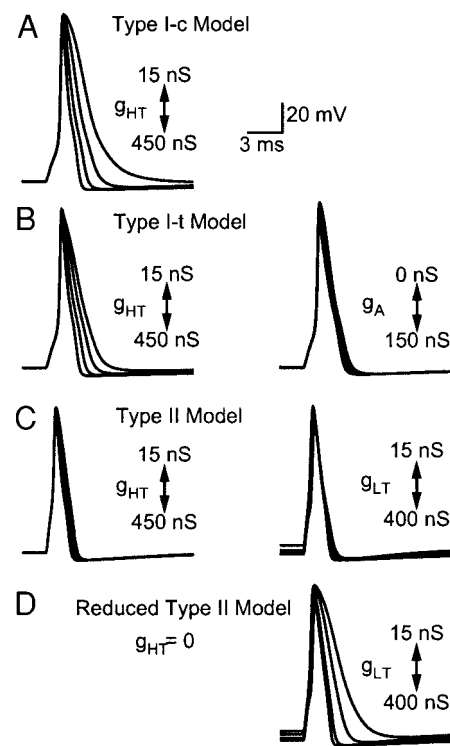


FIG. 10. Model AP repolarization during modulation of  $I_{HT}$  (left) or modulation of  $I_A$  or  $I_{LT}$  (right), for the Type I-c ( $A$ ), Type I-t ( $B$ ), and Type II model ( $C$  and  $D$ ).  $D$ : hypothetical Type II model scenario with no  $I_{HT}$ . APs generated by suprathreshold AN inputs ( $\bar{g}_E = 3\bar{g}_{E0}$ ). Scale bars for all voltage traces.  $T = 22^\circ\text{C}$ .

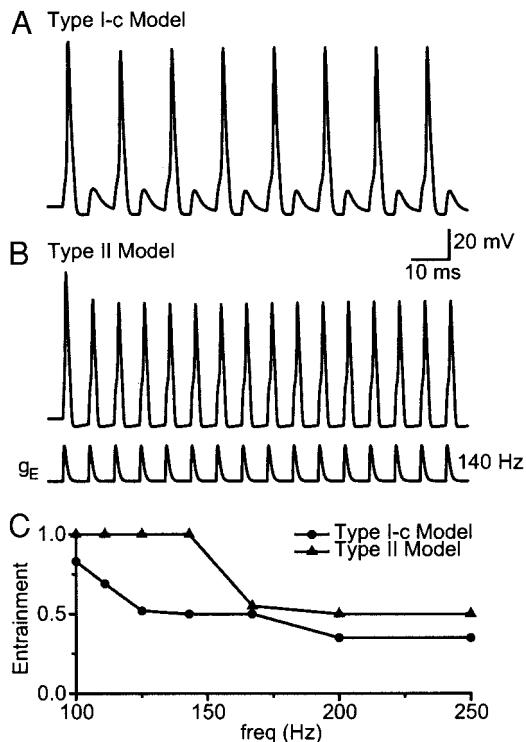


FIG. 9. Model entrainment to suprathreshold inputs. The Type II model ( $B$ ) follows a 140 Hz train of suprathreshold excitatory AN input ( $\bar{g}_E = 3\bar{g}_{E0}$ ) better than the Type I-c model ( $A$ ). Computing entrainment indexes (ratio of input events to output spikes) demonstrates this is true over a range of frequencies ( $C$ ).  $T = 22^\circ\text{C}$ .

contribute to the downstroke of the AP:  $I_{HT}$  and  $I_A$ . However, due to the inactivating behavior of  $I_A$ , and its smaller magnitude, its influence on the rate of repolarization is considerably less than that of  $I_{HT}$  (Fig. 10B). In the Type II model, there are also two  $K^+$  currents that contribute to the downstroke of the AP:  $I_{HT}$  and  $I_{LT}$ . In this case, both  $I_{HT}$  and  $I_{LT}$  repolarize the membrane equally well, in which case modulation of  $I_{HT}$  does not produce a dramatic effect on the rate of repolarization (Fig. 10C, left) nor does modulation of  $I_{LT}$  (right). If, on the other hand,  $I_{HT}$  is removed from the Type II model, then modulation of  $I_{LT}$  produces dramatic changes in the rate of repolarization of the AP (Fig. 10D).

$I_A$  AND  $I_{LT}$  CAN MODULATE THE RATE OF REPETITIVE FIRING. In Fig. 6C, subthreshold EPSPs sum together in time to produce a train of APs spaced at regular intervals. For the same simulation, we found that increasing levels of  $I_A$  ( $\bar{g}_A = 50$ –100 nS) decreased the rate of this repetitive firing by increasing  $\bar{g}_{E0}$ . This is because  $I_A$ , being an outward current, acts to oppose excitatory depolarization (compare Type I-c and Type I-t  $\bar{g}_{E0}$  values in Table 1). When  $\bar{g}_A > 100$  nS,  $\bar{g}_{E0}$  was raised high enough to prevent AP generation. The same effects could be achieved with  $I_{LT}$ , although the conductance levels necessary were significantly smaller ( $\bar{g}_{LT} = 1$ –6 nS). Although similar effects could be achieved by increasing levels of  $I_{HT}$ , the conductance levels necessary to produce the same effects were substantially larger ( $\bar{g}_{HT} = 300$ –1,000 nS), due to  $I_{HT}$ 's higher activation voltage range. Hence, small amounts of  $I_{LT}$ , as well as modest amounts of  $I_A$ , were effective in modulating the rate of repetitive firing in the Type I models.

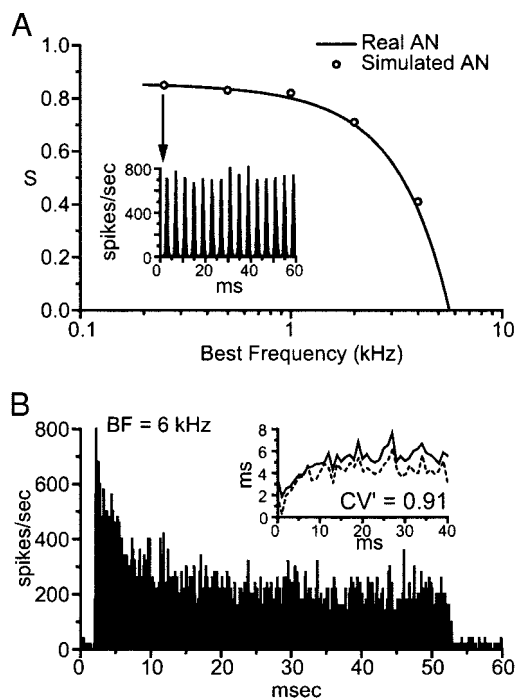


FIG. 11. Simulated AN spike trains. *A*: synchronization indexes ( $S$ ) of simulated AN spike trains ( $\circ$ ), which display phaselocking. —, phaselocking of real AN fibers (Johnson 1980); same line displayed in Fig. 13A of Blackburn and Sachs (1989). *Inset*: poststimulus time histogram (PSTH) of the simulation at 250 Hz (500 trials). The parameters used to simulate these phaselocked spike trains were slightly different from those used by Rothman et al. (1993) and are listed as follows: for  $f = 250, 500, 1,000, 2,000, 4,000$  Hz,  $\varphi = 3.6, 3.1, 3.0, 1.9, 0.8$ , and  $R_{ss} = 1,000, 800, 760, 570, 360$  spikes/s. These parameters were chosen to give sync indexes that match those of Johnson (1980) and to give a mean discharge rate of 150 spikes/s. Because only the steady-state portion of the PSTH was of interest, the adaptation parameters of the AN spike train model were set to zero ( $R_e = 0$  and  $R_{st} = 0$ ); in this way, the entire spike train could be considered as steady state, and therefore included in the synchronization analysis. *B*: PSTH of a simulated AN spike train (500 trials, 0.1-ms bins), resembling that of an AN fiber with both high best frequency (BF:  $f > 5$  kHz) and high spontaneous discharge rate. This spike train was computed with the same parameters used to compute the AN spike train displayed in Fig. 3A of Rothman et al. (1993). *Inset*: regularity analysis (1-ms bins). The mean ( $\mu_{ISI}$ ) and standard deviation ( $\sigma_{ISI}$ ) of the ISI are denoted as — and ---, respectively. For this simulated AN input,  $\mu_{ISI} = 5.71$  ms,  $\sigma_{ISI} = 4.57$  ms,  $ARP = 0.70$  ms,  $CV = 0.80$  and  $CV' = 91$ .

### Model responses to auditory-nerve-like inputs

In this final section, the effects of applying simulated AN inputs to the VCN somatic model are discussed. As described in METHODS, AN inputs are applied by activating the excitatory post-synaptic current,  $I_E$ . Up to this point, the activation time of  $I_E$  has occurred at specified times. In this section, however, the activation time is controlled by a model that accurately describes the spiking discharge pattern of real AN fibers during presentation of pure-tone stimuli. A detailed description of the AN spike generator model has previously been given (Rothman et al. 1993). Further details of the model can be found in the legend of Fig. 11.

**TEMPERATURE SCALING.** Up until now, the operating temperature of the VCN model has been 22°C, the temperature at which most of the in vitro data used in its construction was recorded. In this section, it was of interest to consider the behavior of the model at normal body temperature (38°C) because these results could be compared to in vivo studies.

Hence, to correct for the difference in temperature, all model time constants were multiplied by 0.17 (i.e., a reciprocal Q10 factor of 3) and all peak conductance values (except for  $\bar{g}_E$ ) were multiplied by 3.03 (i.e., a Q10 factor of 2). These Q10 values are approximations to those reported for  $Na^+$  currents (Belluzzi et al. 1985; Sah et al. 1988),  $K^+$  currents (Connor and Stevens 1971a; Frankenhaeuser and Huxley 1964; Hodgkin and Huxley 1952; Kros and Crawford 1990), and excitatory postsynaptic currents (EPSCs) (Zhang and Trussell 1994). The exact Q10 values for peak conductance values in VCN neurons are unknown and therefore are purely speculative at this time.

Inspection of the model current-clamp responses after the preceding temperature corrections shows that, at 38°C, all model types respond to depolarizing current injection as they do at 22°C, except for the intermediate Type II-I model, in which case only very large depolarizing current pulses elicit repetitive firing. Responses to EPSCs are also qualitatively the same as those described at 22°C; however, EPSCs decay at a faster rate ( $\tau_E = 0.4$  ms at 22°C and 0.07 ms at 38°C). Consequently, there is an increase in  $\bar{g}_{E\theta}$  values (see Table 1).

**CONVERGENCE OF AN FIBERS WITH LOW BF (PHASELOCKING).** The AN inputs in this section were patterned after AN fibers with low best frequency (BF; Fig. 11A). Such fibers phaselock to sinusoidal stimuli  $\leq 5$  kHz (Johnson 1980; Joris et al. 1994). To quantify phaselocking, we use the synchronization index ( $S$ ), which takes on values from zero (when all spikes occur randomly throughout the stimulus) to one (when all spikes are synchronized to the stimulus) (Goldberg and Brown 1969).

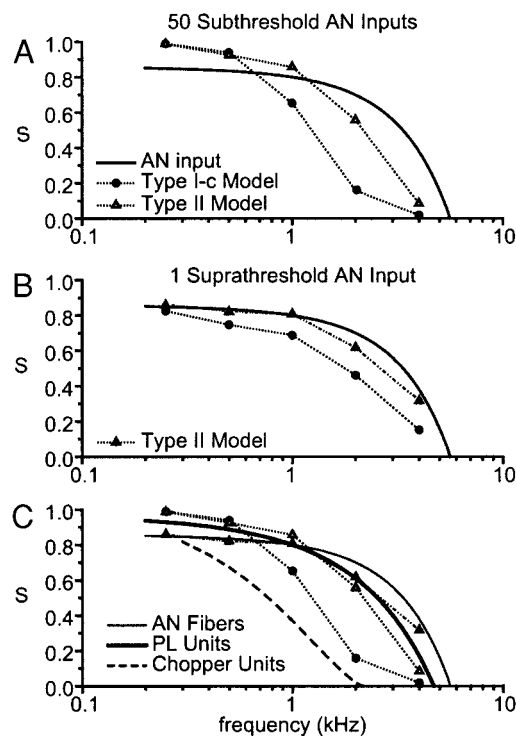


FIG. 12. Model phaselocking. *A*: phaselocking of the Type I-c (circles) and Type II model (open triangles) with 50 subthreshold AN inputs ( $\bar{g}_E = 0.5\bar{g}_{E\theta}$ ). *B*: phaselocking of the Type I-c and Type II (filled triangles) model with 1 suprathreshold AN input ( $\bar{g}_E = 3\bar{g}_{E\theta}$ ). *C*: comparison of the Type I-c model in *A* to chopper units (bold dashed line), and the Type II model in *A* and *B* to primarylike and primarylike-with-notch units (PL; bold solid line). Bold lines are from the VCN data of Blackburn and Sachs (1989), their Fig. 13. Thin line: same AN line in *A* and *B*, and Fig. 11A.  $T = 38^\circ\text{C}$ . Symbols as in *A* and *B*.

Figure 12A shows the results of simulations in which both the Type I-c and Type II model receive 50 subthreshold low-BF AN inputs. Because the AN inputs are subthreshold, summation of two or more EPSPs is required to produce a spike output. At  $f \leq 500$  Hz, both models show phaselocking exceeding that of their AN input ( $S > 0.9$ ). Such “enhanced” phaselocking has been reported in VCN bushy cells (Joris et al. 1994) and is a consequence of converging AN inputs with the same BF. Although enhanced phaselocking can be achieved by a convergence of either subthreshold AN inputs or suprathreshold AN inputs, the highest synchronization with the lowest signal-to-noise ratio is achieved by converging subthreshold AN inputs (Rothman et al. 1993). The mechanism of enhanced phaselocking with converging subthreshold AN inputs is due to the necessity of coincidental inputs to drive a post-synaptic spike: during the peak phase of a sinusoidal stimulus, coincidence of inputs is high, and therefore the output discharge rate is high, whereas during the off-peak phase, coincidence of inputs is near zero, and the output discharge rate is near zero. The end result is higher synchronization in the output than in any one of the AN input.

The fact that the Type I-c model shows enhanced phaselocking at  $f \leq 500$  Hz means that, like the Type II model, it is capable of performing coincidence detection at low frequencies. This is because the average inter-arrival time of the EPSPs at  $f \leq 500$  Hz is sufficiently long ( $\geq 2$  ms) to allow EPSPs to decay to low levels before the arrival of the next EPSP. For  $f > 500$  Hz, however, the EPSP inter-arrival time is  $< 2$  ms, in which case EPSPs sum together to form a steady depolarization of the membrane, inducing repetitive firing (Fig. 6C). Hence, phaselocking in the Type I-c model rapidly degrades at  $f > 500$  Hz (Fig. 12A, circles). The Type II model, in contrast, having such a brief EPSP, is capable of sustaining coincidence detection  $\leq 2$ –3 kHz. For  $f > 1$  kHz, synchronization indexes of the Type II model are comparable to that of its AN input, but not exactly the same (Fig. 12A, triangles).

Model simulations with  $< 50$  subthreshold low-BF AN inputs were also investigated (not shown). In all cases, synchronization indexes were less than that for 50 subthreshold inputs, demonstrating what has previously been reported: the greater the number of converging subthreshold AN inputs, the greater the degree of phaselocking (Rothman and Manis 1996; Rothman and Young 1996; Rothman et al. 1993).

Figure 12B shows the results of simulations in which both the Type I-c and Type II models receive one suprathreshold AN input. In this case, the suprathreshold AN input can produce a spike output whenever the model is not refractory. Hence, these simulations test how well the Type I-c and Type II model follow a suprathreshold AN input one-to-one, as in Fig. 9. Not surprisingly, the Type II model, having the shorter RP, is capable of following the suprathreshold AN input one-to-one better than the Type I-c model at all frequencies. Again, for  $f > 1$  kHz, synchronization indexes of the Type II model are comparable to those of its AN input, but not exactly the same.

Model simulations with more than one suprathreshold AN input were also investigated (not shown). These simulations demonstrate that, for all model types, increasing the number of suprathreshold inputs degrades phase locking at  $f \geq 500$  Hz but enhances phase locking at  $f < 500$  Hz. The enhancement of phaselocking at low frequencies with suprathreshold inputs is

due to convergence of several AN inputs with similar BF, as noted previously (Rothman and Young 1996). However, the number of suprathreshold AN inputs necessary to achieve enhanced phase locking comparable to that seen in real VCN neurons is unusually (and perhaps unrealistically) high:  $\geq 10$ . If one considers no more than five suprathreshold inputs, then the added benefit of having more than one suprathreshold input at low frequencies is small.

When the results in Fig. 12, A and B, are compared to those of real VCN neurons (C), one sees two important similarities. First, the degradation of phaselocking at  $f > 500$  Hz in the Type I-c model with all subthreshold AN inputs parallels the degradation seen in VCN chopper units (Blackburn and Sachs 1989), which are stellate cells (i.e. Type I cells). However, phaselocking is noticeably better in the Type I-c model than in the VCN chopper units at all frequencies. The discrepancy could be due to a difference in membrane properties; however, the more likely explanation is a difference in placement of AN synapses: whereas the Type I-c model receives its AN inputs on its soma, the VCN chopper units are likely to receive their AN inputs on their dendrites (Cant 1981), in which case there would be significant dendritic filtering of the AN inputs and therefore a larger degradation in phaselocking (Banks and Sachs 1991; White et al. 1994).

The second similarity between the real and simulated data is that phaselocking of the Type II model (with both subthreshold and suprathreshold AN inputs) parallels that of VCN bushy cells (Blackburn and Sachs 1989; Joris et al. 1994). Specifically, at  $f < 1$  kHz, both the Type II model and real bushy cells show phaselocking equal to and greater than AN fibers, and at  $f > 1$  kHz, both the Type II model and real bushy cells show phaselocking slightly below that of AN fibers (Fig. 12C). This time there is little discrepancy between the Type II model and real bushy cells.

Simulations with phaselocked AN input were also computed for the Type I-t and intermediate models (not shown). Results of these simulations demonstrate that the Type I-t model phase-locks nearly the same as the Type I-c model and the intermediate models phaselock between that of the Type I-c and Type II models.

**CONVERGENCE OF AN FIBERS WITH HIGH BF (PSTHS AND REGULARITY).** Presented in this section are results from model simulations with non-phaselocked AN inputs (Fig. 11B; BF = 6 kHz). As in the previous section, the analysis was broken into two scenarios of converging AN input: sub- versus suprathreshold. Because neither the input nor output are phaselocked to a sinusoidal stimuli, we present results in the form of PSTHS, which plot the model's instantaneous discharge rate versus time, as well as regularity analysis, which plots the mean ( $\mu_{ISI}$ ) and standard deviation ( $\sigma_{ISI}$ ) of the model's inter-spike interval (ISI) versus time (see Fig. 11B). A common measure of regularity is the coefficient of variation:  $CV = \sigma_{ISI}/\mu_{ISI}$ . For a deadtime-modified Poisson process,  $\sigma_{ISI} = \mu_{ISI} - ARP$ , where ARP is the absolute refractory period (Goldberg et al. 1964), in which case  $CV = 1 - ARP/\mu_{ISI}$ . Hence an increase in the ARP, without any other change in the underlying Poisson process, will cause an unexpected increase in CV. A better measure of regularity, therefore, is CV-prime ( $CV'$ ), which corrects for refractoriness of the spike generator (Rothman et al. 1993):  $CV' = \sigma_{ISI}/(\mu_{ISI} - ARP)$ . In this way,



spike generators with noticeably different refractory characteristics can be compared directly. For the AN spike train in Fig. 11B,  $CV' = 0.91$  (ARP = 0.7 ms), a value comparable to that of real AN fibers (Rothman et al. 1993).

Figure 13 shows a summary of the results for the Type I-c (top) and Type II (bottom) model simulations. On the left appear the model PSTHs when all AN inputs are subthreshold ( $\bar{g}_E = 0.5\bar{g}_{E0}$ ), and on the right appear the model PSTHs when all AN inputs are suprathreshold ( $\bar{g}_E = 3\bar{g}_{E0}$ ). These model PSTHs are meant to be representative of a variety of scenarios, described as follows.

1) The Type I-c model with a large number of subthreshold AN inputs exhibits a “chopping” response (e.g., 50 subthreshold inputs). In this case, inputs from many asynchronous subthreshold AN synapses sum together to produce a large steady depolarization of the model’s membrane potential, resulting in a regular discharge of APs, similar to that in Fig. 6C. The regular discharge of APs results in a PSTH with successive peaks at the onset of the stimulus (i.e., chopping), where the model tends to fire consistently at the same time from trial to trial. The peaks gradually disappear as the model tends to fire less consistently from trial to trial due to the stochastic nature of the AN inputs. The regular discharge of APs also results in a very narrow interspike interval distribution, evident in the small values of  $\sigma_{ISI}$  throughout the stimulus. Hence,  $CV'$  is significantly smaller (0.45) in comparison to the AN inputs (0.91).

2) The Type I-c model with a small number of subthreshold AN inputs exhibits an onset response (e.g., 10 subthreshold inputs). In this case, the number of converging inputs is not enough to induce a significant amount of repetitive firing during the 50-ms stimulus period. Nevertheless, there is a small secondary peak in the PSTH, and the discharge is regular ( $CV' = 0.44$ ).

3) The Type II model with both a large and small number of subthreshold AN inputs exhibits an onset response (e.g., 10 and

50 subthreshold inputs). In this case, a fast  $\tau_m$  and strong outward rectification prevent the asynchronous subthreshold AN inputs from summing, as demonstrated in Fig. 6C; hence, there is very little spike activity during the steady-state portion of the stimulus (<100 spikes/s), even with a large number of AN inputs. There is, however, a near-instantaneous change of rate at the onset of the stimulus due to a large number of coincidental inputs at this time. The variance of this initial onset response is similar to that of the Type I-c onset response. The Type II and Type I-c onset responses are distinguishable by their regularity: the Type II onset responses, for either 10 or 50 subthreshold AN inputs, are more irregular ( $CV' = 0.58$  and 0.69, respectively) than the Type I-c onset responses ( $CV' = 0.44$  and 0.45, respectively).

4) The Type I-c model with one suprathreshold AN input exhibits a primarylike-with-notch (“Pri-notch”) response. In this case, a long RP prevents the model from following its suprathreshold input one-to-one. The result is not only a reduction in the steady-state discharge rate, but a notch in the PSTH following the initial onset response. The notch occurs because the suprathreshold AN input forces the model to discharge at the beginning of the stimulus for almost every trial, in which case the ensuing RP prevents the model from spiking again until ~4 ms later. Interestingly, a comparison of CV values seems to suggest the model’s output is regular in comparison to its input ( $CV = 0.51$  and 0.80, respectively). However, a comparison of  $CV'$  values shows the model’s output is actually as irregular as its input ( $CV' = 0.96$  and 0.91, respectively), demonstrating how a simple change in refractoriness can make an irregular process appear regular when using CV as a measure of regularity.

5) The Type II model with one suprathreshold AN input exhibits a “primarylike” response. In this case, a short RP allows the model to follow the suprathreshold input better than the Type I-c model. There is no notch following the initial onset response, and the steady-state discharge rate is closer to

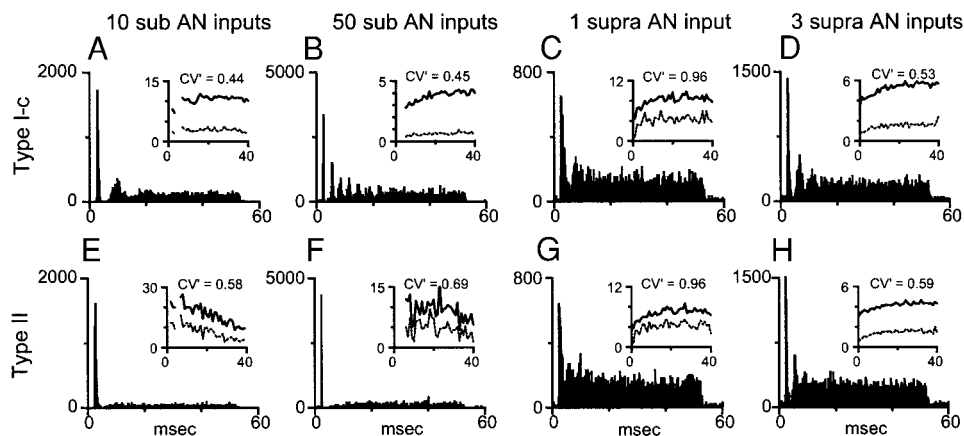


FIG. 13. PSTHs and regularity analysis (insets) of the Type I-c (top) and Type II model (bottom) in response to 10 and 50 subthreshold AN inputs (left and middle left,  $\bar{g}_E = 0.5\bar{g}_{E0}$ ), and in response to 1 and 3 suprathreshold AN inputs (right and middle right,  $\bar{g}_E = 3\bar{g}_{E0}$ ). The PSTH of each AN input resembles the one in Fig. 11B. y axis of the PSTHs is in units of spikes/s. x and y axis of the regularity plots are in units of ms. Data analysis is the same as that in Fig. 11B. A:  $\mu_{ISI} = 11.05$  ms,  $\sigma_{ISI} = 2.98$  ms, ARP = 4.35 ms, CV = 0.27 and  $CV' = 0.44$ . B:  $\mu_{ISI} = 3.90$  ms,  $\sigma_{ISI} = 0.61$  ms, ARP = 2.55 ms, CV = 0.16 and  $CV' = 0.45$ . C:  $\mu_{ISI} = 8.64$  ms,  $\sigma_{ISI} = 4.42$  ms, ARP = 4.05 ms, CV = 0.51 and  $CV' = 0.96$ . D:  $\mu_{ISI} = 5.53$  ms,  $\sigma_{ISI} = 1.59$  ms, ARP = 2.55 ms, CV = 0.29 and  $CV' = 0.53$ . E:  $\mu_{ISI} = 16.53$  ms,  $\sigma_{ISI} = 7.32$  ms, ARP = 3.75 ms, CV = 0.44 and  $CV' = 0.58$ . F:  $\mu_{ISI} = 10.10$  ms,  $\sigma_{ISI} = 5.25$  ms, ARP = 2.45 ms, CV = 0.52 and  $CV' = 0.69$ . G:  $\mu_{ISI} = 7.37$  ms,  $\sigma_{ISI} = 4.64$  ms, ARP = 2.55 ms, CV = 0.63 and  $CV' = 0.96$ . H:  $\mu_{ISI} = 4.28$  ms,  $\sigma_{ISI} = 1.56$  ms, ARP = 1.65 ms, CV = 0.37 and  $CV' = 0.59$ . The ARP was estimated as the minimum ISI.  $T = 38^\circ\text{C}$ .

that of the AN input. Again, due to the effects of refractoriness, the output appears more regular than the AN input when comparing CV values ( $CV = 0.63$  and  $0.80$ , respectively) but just as irregular when comparing  $CV'$  values ( $CV' = 0.96$  and  $0.91$ , respectively).

6) The Type I-c model with several suprathreshold AN inputs exhibits a chopping response (e.g., 3 suprathreshold inputs). This scenario is similar to the one with converging subthreshold AN inputs except there is less temporal precision in the output spike train. In comparison to the model's response to converging subthreshold inputs, for example, the model's response to converging suprathreshold inputs shows a less precisely timed onset response, fewer peaks following the onset response, and a larger  $\sigma_{ISI}$ .

7) The Type II model with several suprathreshold AN inputs exhibits a Pri-notch response (e.g., 3 suprathreshold inputs). In this case, convergence of more than one suprathreshold input forces the model to fire at the onset of the stimulus more precisely than if there was just one input. Because the model is refractory for  $\sim 1.7$  ms after the initial onset spike, a notch appears in the PSTH. A comparison of  $CV'$  values shows that as the number of suprathreshold inputs increases, the Type II model becomes more regular (for 3 suprathreshold inputs,  $CV' = 0.59$ , for 5 suprathreshold inputs,  $CV' = 0.40$ ). Here, the increase in regularity is due to the fact that, with several suprathreshold AN inputs, the model tends to fire the moment it is no longer refractory. The end result is a narrow interspike interval distribution, or small  $\sigma_{ISI}$ . Therefore, increasing the number of suprathreshold AN inputs decreases  $CV'$ , as reported by Rothman et al. (1993).

The same simulations in Fig. 13 were also computed for the Type I-t model and the two intermediate models (not shown). Results from these simulations show that with respect to PSTHs and regularity, the Type I-t model is nearly indistinguishable from the Type I-c model, and, the intermediate models fall between the Type I-c and Type II models, where the Type I-II model appears more like the Type I-c model, and the Type II-I model appears more like the Type II model. However, with respect to classification based on PSTH appearance, most of the intermediate responses have Pri-notch appearances.

**MODULATION OF  $I_h$  ENHANCES TEMPORAL ACUITY IN THE TYPE II MODEL.** As demonstrated in Fig. 7B, a shift in activation of  $I_h$  causes a reduction in EPSP width and amplitude of the Type II model EPSP. It was hypothesized that this could enhance coincidence detection. To test this hypothesis further, simulations of the Type II model with converging subthreshold high-BF AN inputs (Fig. 11B) were compared before and after a positive shift in activation of  $I_h$ . Because the AN inputs were subthreshold in these simulations, the Type II model was acting as an EPSP coincidence detector. Results are shown in Fig. 14, where model PSTHs before and after the 15-mV shift in  $I_h$  (+NE) are plotted. Here, a comparison of PSTHs reveals three changes due to the shift in  $I_h$ : a more precisely timed onset response, a lower sustained discharge rate, and a lower spontaneous discharge rate. Because the probability of coincidence is high at the onset of the stimulus, but low everywhere else (especially before and after the stimulus), these results are expected for a mechanism that enhances coincidence detection.

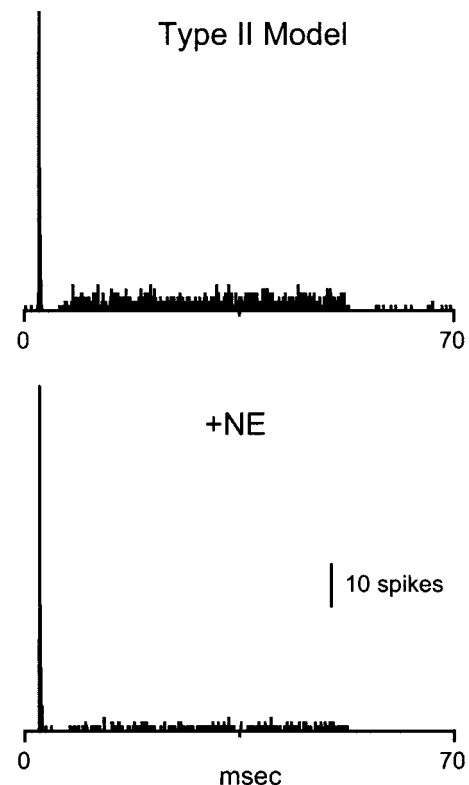


FIG. 14. Modulation of  $I_h$  enhances temporal acuity. Type II model PSTH before (left) and after (right) a shift in half-activation of  $I_h$ , as in Fig. 7B (+NE). For both simulations, the model received 20 subthreshold AN inputs, similar to that in Fig. 11B.  $T = 38^\circ\text{C}$ .

## DISCUSSION

In this paper we present a robust model of VCN neurons based on our previous experimental findings (Rothman and Manis 2003a,b). This model replicates many of the complex behaviors associated with VCN neurons, including the Type I current-clamp response of stellate cells and the Type II current-clamp response of bushy cells. The model also replicates many of the PSTH, regularity and phaselocking responses associated with these neurons. Although previous models have achieved similar success in replicating the behavior of VCN neurons (see INTRODUCTION), the current model presented here is considered more accurate because it was derived from a complete characterization of the  $K^+$  currents, rather than ad hoc assumptions. The largest difference between the models is in the voltage dependence of the high-threshold  $K^+$  current ( $I_{HT}$ ) and the magnitude of the low-threshold current ( $I_{LT}$ ). In most previous models, these two currents were confounded, such that  $I_{HT}$  behaved more like  $I_{LT}$ , limiting the interpretation of the relative roles of the currents, especially with respect to VCN bushy cells. In the future, it will be important to characterize the behavior of  $I_{Na}$  and  $I_h$  in VCN neurons, since our characterizations of these two currents were derived from other neurons.

### Functional significance of $I_A$

Since the discovery of the fast transient  $K^+$  current ( $I_A$ ) in crab (Connor and Stevens 1971b) and molluscan neurons (Hagiwara et al. 1961),  $I_A$  has been localized to a variety of

neurons that display repetitive firing (Rudy 1988). Similarly, we find  $I_A$  only in our population of Type I cells, i.e., the stellate cells, which are thought to encode their output in repetitive firing. Hence,  $I_A$  may play a role in modulating the rate of repetitive firing in VCN stellate cells. Our modeling simulations indicate  $I_A$  could in fact play such a role. In these simulations, increasing levels of  $I_A$  counteracted the depolarizing effects of excitatory synaptic input, thereby increasing the threshold of AP generation. The end result was a decrease in discharge rate. When the magnitude of  $I_A$  was large enough, repetitive firing was abolished altogether.

These conclusions are somewhat different from those of  $I_A$  in the dorsal cochlear nucleus (Kanold and Manis 1999, 2001). However, neurons with  $I_A$  in the dorsal cochlear nucleus show a more complex discharge pattern than VCN Type I cells, suggesting  $I_A$  plays different roles in the two sets of cells.  $I_A$  in the dorsal cochlear nucleus in fact shows considerable difference in activation/inactivation kinetics in comparison to  $I_A$  in VCN neurons, again suggesting two distinct fast-inactivating  $K^+$  currents.

In future modeling studies it will be important to also simulate the nature of inhibitory inputs to Type I cells because hyperpolarization of their membrane will produce a dramatic effect on the magnitude of  $I_A$  due to the de-inactivation that occurs in the voltage range above and below their resting membrane potential.

#### Functional significance of $I_{HT}$

Results from our modeling simulations indicate  $I_{HT}$  is primarily responsible for repolarizing the membrane during the downstroke of an AP. The one exception is when  $I_{HT}$  and  $I_{LT}$  are "expressed" together, in which case both  $I_{HT}$  and  $I_{LT}$  act to repolarize the membrane. In fact,  $I_{LT}$  repolarizes the membrane nearly as well as  $I_{HT}$ . Why would a cell, then, express both  $I_{HT}$  and  $I_{LT}$ , if  $I_{LT}$  alone is sufficient to repolarize the membrane? One possibility is that  $I_{HT}$  functions as the steadfast means of repolarizing the membrane during periods of modulation of  $I_{LT}$ . As Fig. 10D demonstrates, in the absence of  $I_{HT}$ , modulation of  $I_{LT}$  produces a dramatic effect on the rate of repolarization during an AP. This is not true when  $I_{HT}$  is present (Fig. 10C). Why a cell might need to modulate  $I_{LT}$  is discussed in the following text.

It was previously suggested that  $I_{HT}$  in bushy cells contributes to the precise conveyance of rapid temporal information (Perney and Kaczmarek 1997; Wang et al. 1998). This hypothesis stemmed from modeling results that showed  $I_{HT}$  significantly reduced the duration of "large" EPSPs and  $I_{HT}$  allowed a bushy cell model to follow a high-frequency train of synaptic inputs (100–600 Hz), which was otherwise not possible when  $I_{HT}$  was absent. However, the simulations that demonstrate  $I_{HT}$ 's ability to improve phaselocking at high frequencies are problematic. In these simulations, the maximum conductance of  $I_{HT}$  was set to an unusually large value (50  $\mu$ S), in which case  $I_{HT}$  activated at potentials near  $-60$  mV (see Fig. 1,  $I_{HT}$ , trace 2). Hence,  $I_{HT}$  in these simulations can no longer be considered high threshold but rather low threshold. In addition, the large EPSPs that showed significant reduction in duration with increasing levels of  $I_{HT}$  were suprathreshold EPSPs with peak amplitude near 0 mV. Such large EPSPs would normally elicit APs and would therefore not be directly observed in real

bushy cells. These large EPSPs did not elicit APs in the model because the  $Na^+$  current was removed from the simulations. The reduction in width of these very large EPSPs confirms the finding that, at suprathreshold potentials ( $V > -50$  mV),  $I_{HT}$  contributes to repolarization of the membrane, as it does during the course of an AP. These results are however consistent with the idea that  $I_{LT}$  makes the major contribution to the precise conveyance of rapid temporal information.

#### Functional significance of $I_{LT}$

The modeling results in this paper suggest several functions of  $I_{LT}$ . The most noteworthy of these functions is in reducing the membrane time constant ( $\tau_m$ ) at subthreshold potentials. By far, of all the currents investigated in this study,  $I_{LT}$  was most adept at reducing  $\tau_m$  in the range  $-70$  to  $-50$  mV. Perhaps the best illustration of  $I_{LT}$ 's ability in reducing  $\tau_m$  is in Fig. 7A, which shows the model's response to a subthreshold synaptic input with and without  $I_{LT}$ . Here, the ability of  $I_{LT}$  to reduce  $\tau_m$  is clearly reflected in the difference in decay rate of the two EPSPs. These results suggest a neuron acting as an EPSP coincidence detector would be well served to express  $I_{LT}$  because  $I_{LT}$  greatly reduces the width of subthreshold EPSPs, thereby shortening the window over which EPSPs sum together. The next best illustration of  $I_{LT}$ 's ability in reducing  $\tau_m$  at subthreshold potentials is given in Fig. 8, B and C. Here, the ability of  $I_{LT}$  to reduce  $\tau_m$  is reflected in the reduction of the refractory period after the addition of  $I_{LT}$  to the model. Hence a neuron that aspires to follow its synaptic input at very fast rates would also be well served to express  $I_{LT}$ .

There are two additional roles for  $I_{LT}$ . First,  $I_{LT}$  could modulate the rate of repetitive firing, similar to the role proposed for  $I_A$ . Our modeling results show that small amounts of  $I_{LT}$  produce a dramatic change in the rate of repetitive firing, and these effects are qualitatively indistinguishable from the changes produced by larger values of  $I_A$ . Neurons that encode their output in the form of repetitive firing might be well served to express small amounts of  $I_{LT}$ . One potential advantage of utilizing  $I_{LT}$  is its relatively weak inactivation voltage dependence, which will limit the kind of behavior that can be produced by rapidly inactivating  $I_A$  currents (Kanold and Manis 1999, 2001). Second,  $I_{LT}$  could potentially change suprathreshold events into subthreshold events. For example, neurons that express  $I_{LT}$  in the initial segment of their axons or proximal dendrites might have much more limited back-propagation of APs into the dendritic tree.

#### Modulation of $I_{LT}$

All of the preceding functions of  $I_{LT}$  could easily be regulated by modulating the activation level of  $I_{LT}$ . An upregulation of  $I_{LT}$ , for example, would cause a further reduction in  $\tau_m$ , thereby reducing the width and amplitude of EPSPs. For a neuron acting as an EPSP coincidence detector, the reduction in width and amplitude of EPSPs would lead to an enhancement of temporal acuity; that is, an increase in precision of spike occurrences during the peak phase of a stimulus, and a decrease in spike occurrences during the off-peak phase, including periods of spontaneous activity (Fig. 14). A reduction in  $\tau_m$  would also lead to a reduction in the refractory period following an AP, thereby allowing a neuron to fire at a higher



discharge rate. Hence an upregulation of  $I_{LT}$  would boost a neuron's ability to preserve and even enhance the temporal encoding of its synaptic inputs.

A simple means of upregulating the activation level of  $I_{LT}$  would be to simply increase  $I_{LT}$ , by either increasing its peak conductance or removing its inactivation. However, increasing  $I_{LT}$  leads to a concomitant hyperpolarization of the resting membrane potential ( $V_{rest}$ ) toward the  $K^+$  reversal potential because the increase in  $I_{LT}$ , an outward current, is not opposed by an increase in an inward current ( $V_{rest}$  is the potential where the sum total of outward currents is counterbalanced by the sum total of inward currents). In other words,  $V_{rest}$  moves to more hyperpolarized potentials to deactivate  $I_{LT}$ . The end result is the same steady-state activation level of  $I_{LT}$ , now at a lower  $V_{rest}$ . As investigated in Fig. 7, a possible solution to this problem rests with the hyperpolarization-activated cation current ( $I_h$ ). Because  $I_h$  is an inward current below  $-40$  mV, it serves to counterbalance the hyperpolarizing force of  $I_{LT}$ . To increase the activation level of  $I_{LT}$ , then, a neuron might increase  $I_h$  because an increase in  $I_h$  leads to a concomitant depolarization of  $V_{rest}$ , which in turn leads to an increase in activation of  $I_{LT}$ . The end result is a larger activation level of  $I_{LT}$ , and a slightly higher  $V_{rest}$ . Or, a neuron might increase both  $I_{LT}$  and  $I_h$  simultaneously in order to increase the activation level of  $I_{LT}$  without significantly changing  $V_{rest}$ .

The hypothesis that  $I_h$  is used as a means of modulating  $I_{LT}$  by changing  $V_{rest}$  was proposed by Banks et al. (1993). In their study, Banks et al. found that  $I_h$  in MNTB neurons is modulated by norepinephrine (NE) as well as a membrane permeable analogue of cyclic-AMP (8-Br-cAMP). If  $I_h$  in VCN neurons is similar to  $I_h$  in MNTB neurons, then it might be possible that NE and/or cyclic-AMP act to modulate  $I_h$  in VCN neurons. If  $I_{LT}$  is also modulated by cAMP, the effects could be synergistic with modulation if  $I_h$ . There is some evidence in expression systems that KCNA1 (a likely component of  $I_{LT}$ ) (see Rothman and Manis 2003b) can be regulated by phosphorylation by cyclic-AMP-dependent kinases (Ivanina et al. 1994; Levin et al. 1995; Matthias et al. 2002), with a resulting increase in current through the channels at a given voltage. Whether this occurs in native channels remains to be determined.

Interestingly, an *in vivo* study of bat VCN neurons found that iontophoretic application of NE during acoustic stimulation enhanced the onset response of these neurons as well as decreased the sustained and spontaneous discharge rates (Kossel and Vater 1989). The cells under investigation were located in the anterior region of the VCN and often exhibited "primary-like" responses to tone bursts, suggesting these cells were bushy cells or Type II cells. Hence, it is possible that NE was acting on  $I_h$  (and possibly  $I_{LT}$ ) in these VCN neurons, as it did in MNTB neurons.

### Implications for bushy cells

An interesting distinction between bushy cells in the VCN is the size and number of their AN inputs. Spherical bushy cells, for example, receive a small number of endbulbs of Held (1 or 2), which presumably form secure (i.e. suprathreshold) synapses. In the most rostral region of the VCN, spherical bushy cells are contacted by a single endbulb of Held (Ryugo and Sento 1991). With such an exclusive suprathreshold input, these cells are poised to act as relay cells from the cochlear

nucleus to the superior olivary complex. The only condition preventing a spherical bushy cell from acting as a relay cell would be a long post-synaptic refractory period. Spherical bushy cells, therefore, appear to express high levels of  $I_{LT}$  to help reduce the refractory period following an AP. In this way, spherical bushy cells are able to follow their suprathreshold AN input one-to-one better than if they did not express  $I_{LT}$  (see Fig. 9).

The expression of large  $I_{LT}$  in spherical bushy cells comes with a cost, however: a reduction in synaptic efficacy. This is evident in Fig. 7, which shows the effect of  $I_{LT}$  is not only to decrease the width of an EPSP but its height as well. One solution to this problem is to increase the synaptic conductance. Results from this study indicate that, for every additional 50 nS of  $\bar{g}_{LT}$  added to an excitable membrane, the peak synaptic conductance has to be increased by  $\sim 75\%$  to keep synaptic efficacy constant ( $T = 22^\circ\text{C}$ ). This might explain why spherical bushy cells receive such unusually large synapses from AN fibers, the endbulbs of Held, with many active zones.

In contrast to spherical bushy cells, globular bushy cells receive a large number of small AN inputs. The difference in AN input configuration between spherical and globular bushy cells clearly suggests a difference in function. Indeed, comparison of the temporal response patterns between spherical and globular bushy cells demonstrates that globular bushy cells have a more precisely timed onset response, and an enhanced ability to phaselock to a sinusoidal stimulus (Blackburn and Sachs 1989; Joris et al. 1994). How globular bushy cells achieve this "enhancement" of timing can be explained by a coincidence detection model, whereby coincidence of two or more excitatory inputs is necessary to generate an output spike (Joris et al. 1994; Rothman et al. 1993). Not surprisingly, the best coincidence detectors are those with a large number of inputs, each of which produces a small, brief EPSP. Globular bushy cells, therefore, appear to express high levels of  $I_{LT}$ , not only to reduce the refractory period following an AP, but to reduce the width of subthreshold EPSPs. In this way, globular bushy cells are able to act as coincidence detectors far better than if they did not express  $I_{LT}$ .

### APPENDIX: MODEL EQUATIONS

The model currents presented below have voltage and time dependencies similar to those of the original Hodgkin and Huxley model (1952). In these equations, currents are governed by an activation/inactivation variable  $x$  whose rate of change is defined by the following first-order differential equation

$$\frac{dx}{dt} = (x_\infty - x)/\tau_x \quad (A1)$$

where  $\tau_x$  is the time constant of  $x$ ,  $x_\infty$  is the steady-state value of  $x$  (i.e. the value of  $x$  when  $t \gg \tau_x$ ), and  $x$  itself represents the activation/inactivation variables  $a$ ,  $b$ ,  $c$ ,  $w$ ,  $z$ ,  $n$ ,  $p$ ,  $m$ ,  $h$ , and  $r$  in the following text. Although the formalism of the preceding equation is different from the original HH formalism in which activation/inactivation variables are expressed in terms of "open" and "close" rate constants  $\alpha$  and  $\beta$ , they are nevertheless mathematically equivalent when  $x_\infty = \alpha/(\alpha + \beta)$  and  $\tau_x = 1/(\alpha + \beta)$ . Reversal potentials are:  $V_K = -70$  mV,  $V_{Na} = +55$  mV,  $V_h = -43$  mV, and  $V_{Ik} = -65$  mV.

**Fast transient  $K^+$  current**

$$I_A = \bar{g}_A \cdot a^4 bc \cdot (V - V_k) \quad (A2)$$

$$a_\infty = [1 + \exp(-(V + 31)/6)]^{-1/4} \quad (A3)$$

$$b_\infty = [1 + \exp((V + 66)/7)]^{-1/2} \quad (A4)$$

$$c_\infty = b_\infty \quad (A5)$$

$$\tau_a = 100 \cdot [7 \exp((V + 60)/14) + 29 \exp(-(V + 60)/24)]^{-1} + 0.1 \quad (A6)$$

$$\tau_b = 1000 \cdot [14 \exp((V + 60)/27) + 29 \exp(-(V + 60)/24)]^{-1} + 1 \quad (A7)$$

$$\tau_c = 90 \cdot [1 + \exp(-(V + 66)/17)]^{-1} + 10 \quad (A8)$$

**Low-threshold  $K^+$  current**

$$I_{LT} = \bar{g}_{LT} \cdot w^4 z \cdot (V - V_k) \quad (A9)$$

$$w_\infty = [1 + \exp(-(V + 48)/6)]^{-1/4} \quad (A10)$$

$$z_\infty = (1 - \zeta) \cdot [1 + \exp((V + 71)/10)]^{-1} + \zeta \quad (\zeta = 0.5) \quad (A11)$$

$$\tau_w = 100 \cdot [6 \exp((V + 60)/6) + 16 \exp(-(V + 60)/45)]^{-1} + 1.5 \quad (A12)$$

$$\tau_z = 1000 \cdot [\exp((V + 60)/20) + \exp(-(V + 60)/8)]^{-1} + 50 \quad (A13)$$

**High-threshold  $K^+$  current**

$$I_{HT} = \bar{g}_{HT} \cdot [\varphi n^2 + (1 - \varphi)p] \cdot (V - V_k) \quad (\varphi = 0.85) \quad (A14)$$

$$n_\infty = [1 + \exp(-(V + 15)/5)]^{-1/2} \quad (A15)$$

$$p_\infty = [1 + \exp(-(V + 23)/6)]^{-1} \quad (A16)$$

$$\tau_n = 100 \cdot [11 \exp((V + 60)/24) + 21 \exp(-(V + 60)/23)]^{-1} + 0.7 \quad (A17)$$

$$\tau_p = 100 \cdot [4 \exp((V + 60)/32) + 5 \exp(-(V + 60)/22)]^{-1} + 5 \quad (A18)$$

**Fast  $Na^+$  current**

$$I_{Na} = \bar{g}_{Na} \cdot m^3 h \cdot (V - V_{Na}) \quad (A19)$$

$$m_\infty = [1 + \exp(-(V + 38)/7)]^{-1} \quad (A20)$$

$$h_\infty = [1 + \exp((V + 65)/6)]^{-1} \quad (A21)$$

$$\tau_m = 10 \cdot [5 \exp((V + 60)/18) + 36 \exp(-(V + 60)/25)]^{-1} + 0.04 \quad (A22)$$

$$\tau_h = 100 \cdot [7 \exp((V + 60)/11) + 10 \exp(-(V + 60)/25)]^{-1} + 0.6 \quad (A23)$$

**Hyperpolarization-activated cation current**

$$I_h = \bar{g}_h \cdot r \cdot (V - V_h) \quad (A24)$$

$$r_\infty = [1 + \exp((V + 76)/7)]^{-1} \quad (A25)$$

$$\tau_r = 10^5 \cdot [237 \exp((V + 60)/12) + 17 \exp(-(V + 60)/14)]^{-1} + 25 \quad (A26)$$

**Leak current**

$$I_{lk} = \bar{g}_{lk} \cdot (V - V_{lk}) \quad (A27)$$

This work was supported by National Institute of Deafness and Other Communication Disorders Grants P60DC-00979 (Research and Training Center in Hearing and Balance), Subproject 2, and R01 DC-04551 to P. B. Manis. J. S. Rothman was also partially supported by Training Grant T32DC-00023.

## REFERENCES

- Arle JE and Kim DO.** Neural modeling of intrinsic and spike-discharge properties of cochlear nucleus neurons. *Biol Cybern* 64: 273–283, 1991.
- Bal R and Oertel D.** Hyperpolarization-activated, mixed-cation current ( $I_h$ ) in octopus cells of the mammalian cochlear nucleus. *J Neurophysiol* 84: 806–817, 2000.
- Bal R and Oertel D.** Potassium currents in octopus cells of the mammalian cochlear nucleus. *J Neurophysiol* 86: 2299–2311, 2001.
- Banks MI, Pearce RA, and Smith PH.** Hyperpolarization-activated cation current ( $I_h$ ) in neurons of the medial nucleus of the trapezoid body: voltage-clamp analysis and enhancement by norepinephrine and cAMP suggest a modulatory mechanism in the auditory brain stem. *J Neurophysiol* 70: 1420–1432, 1993.
- Banks MI and Sachs MB.** Regularity analysis in a compartmental model of chopper units in the anteroventral cochlear nucleus. *J Neurophysiol* 65: 606–629, 1991.
- Barnes-Davies M and Forsythe ID.** Pre- and postsynaptic glutamate receptors at a giant excitatory synapse in rat auditory brainstem slices. *J Physiol* 488: 387–406, 1995.
- Belluzzi O, Sacchi O, and Wanke E.** A fast transient outward current in the rat sympathetic neurone studied under voltage-clamp conditions. *J Physiol* 358: 91–108, 1985.
- Blackburn CC and Sachs MB.** Classification of unit types in the anteroventral cochlear nucleus: PST histograms and regularity analysis. *J Neurophysiol* 62: 1303–1329, 1989.
- Brew HM and Forsythe ID.** Two voltage-dependent  $K^+$  conductances with complementary functions in postsynaptic integration at a central auditory synapse. *J Neurosci* 15: 8011–8022, 1995.
- Cant NB.** The fine structure of two types of stellate cells in the anterior division of the anteroventral cochlear nucleus of the cat. *Neuroscience* 6: 2643–2655, 1981.
- Connor JA and Stevens CF.** Inward and delayed outward membrane currents in isolated neural somata under voltage clamp. *J Physiol* 213: 1–19, 1971a.
- Connor JA and Stevens CF.** Voltage-clamp studies of a transient outward membrane current in gastropod neural somata. *J Physiol* 213: 21–30, 1971b.
- Costa PF.** The kinetic parameters of sodium currents in maturing acutely isolated rat hippocampal CA1 neurons. *Brain Res Dev Brain Res* 91: 29–40, 1996.
- Cuttle MF, Rusznak Z, Wong AY, Owens S, and Forsythe ID.** Modulation of a presynaptic hyperpolarization-activated cationic current ( $I_h$ ) at an excitatory synaptic terminal in the rat auditory brainstem. *J Physiol* 534: 733–744, 2001.
- Francis HW and Manis PB.** Effects of deafferentation on the electrophysiology of ventral cochlear nucleus neurons. *Hear Res* 149: 91–105, 2000.
- Frankenhaeuser B and Huxley A.** The action potential in the myelinated nerve fiber of *Xenopus laevis* as computed on the basis of voltage clamp. *J Physiol* 171: 302–315, 1964.
- Fu XW, Brezden BL, and Wu SH.** Hyperpolarization-activated inward current in neurons of the rat's dorsal nucleus of the lateral lemniscus in vitro. *J Neurophysiol* 78: 2235–2245, 1997.
- Gentet L, Stuart G, and Clements J.** Direct measurement of specific membrane capacitance in neurons. *Biophys J* 79: 314–320, 2000.
- Goldberg JM, Adrian HO, and Smith FD.** Response of neurons of the superior olivary complex of the cat to acoustic stimuli of long duration. *J Neurophysiol* 27: 706–749, 1964.
- Goldberg JM and Brown PB.** Response of binaural neurons of dog superior olivary complex to dichotic tonal stimuli: some physiological mechanisms of sound localization. *J Neurophysiol* 32: 613–636, 1969.
- Hagiwara S, Kusano K, and Saito N.** Membrane changes in *Onchidium* nerve cell in potassium rich media. *J Physiol* 155: 470–489, 1961.
- Hewitt MJ, Meddis R, and Shackleton TM.** A computer model of a cochlear-nucleus stellate cell: responses to amplitude-modulated and pure-tone stimuli. *J Acoust Soc Am* 91: 2096–2109, 1992.
- Hodgkin AL and Huxley AF.** A quantitative description of membrane current and its application to conduction and excitation in nerve. *J Physiol* 117: 500–544, 1952.
- Huguenard JR and McCormick DA.** Simulation of the currents involved in rhythmic oscillations in thalamic relay neurons. *J Neurophysiol* 68: 1373–1383, 1992.
- Isaacson JS and Walmsley B.** Receptors underlying excitatory synaptic transmission in slices of the rat anteroventral cochlear nucleus. *J Neurophysiol* 73: 964–973, 1995.
- Ivanina T, Perets T, Thornhill WB, Levin G, Dascal N, and Lotan I.** Phosphorylation by protein kinase A of RCK1  $K^+$  channels expressed in *Xenopus* oocytes. *Biochemistry* 33: 8786–8792, 1994.

- Johnson DH.** The relationship between spike rate and synchrony in responses of auditory-nerve fibers to single tones. *J Acoust Soc Am* 68: 1115–1122, 1980.
- Joris PX, Carney LH, Smith PH, and Yin TC.** Enhancement of neural synchronization in the anteroventral cochlear nucleus. I. Responses to tones at the characteristic frequency. *J Neurophysiol* 71: 1022–1036, 1994.
- Kanemasa T, Gan L, Perney TM, Wang LY, and Kaczmarek LK.** Electrophysiological and pharmacological characterization of a mammalian Shaw channel expressed in NIH 3T3 fibroblasts. *J Neurophysiol* 74: 207–217, 1995.
- Kanold PO and Manis PB.** Transient potassium currents regulate the discharge patterns of dorsal cochlear nucleus pyramidal cells. *J Neurosci* 19: 2195–2208, 1999.
- Kanold PO and Manis PB.** A physiologically based model of discharge pattern regulation by transient  $K^+$  currents in cochlear nucleus pyramidal cells. *J Neurophysiol* 85: 523–538, 2001.
- Kossel M and Vater M.** Noradrenaline enhances temporal auditory contrast and neuronal timing precision in the cochlear nucleus of the mustached bat. *J Neurosci* 9: 4169–4178, 1989.
- Kros CJ and Crawford AC.** Potassium currents in inner hair cells isolated from the guinea pig cochlea. *J Physiol* 421: 263–291, 1990.
- Levin G, Keren T, Peretz T, Chikvashvili D, Thornhill WB, and Lotan I.** Regulation of RCK1 currents with a cAMP analog via enhanced protein synthesis and direct channel phosphorylation. *J Biol Chem* 270: 14611–14618, 1995.
- Manis PB and Marx SO.** Outward currents in isolated ventral cochlear nucleus neurons. *J Neurosci* 11: 2865–2880, 1991.
- Matthias K, Seifert G, Reinhardt S, and Steinhauser C.** Modulation of voltage-gated  $K^+$  channels Kv1.1 and Kv1.4 by forskolin. *Neuropharmacology* 43: 444–449, 2002.
- Oertel D.** Synaptic responses and electrical properties of cells in brain slices of the mouse anteroventral cochlear nucleus. *J Neurosci* 3: 2043–2053, 1983.
- Oertel D.** The role of intrinsic neuronal properties in the encoding of auditory information in the cochlear nuclei. *Curr Opin Neurobiol* 1: 221–228, 1991.
- Ogata N and Tatebayashi H.** Kinetic analysis of two types of  $Na^+$  channels in rat dorsal root ganglia. *J Physiol* 466: 9–37, 1993.
- Parri HR and Crunelli V.** Sodium current in rat and cat thalamocortical neurons: role of a noninactivating component in tonic and burst firing. *J Neurosci* 18: 854–867, 1998.
- Perney TM and Kaczmarek LK.** Localization of a high threshold potassium channel in the rat cochlear nucleus. *J Comp Neurol* 386: 178–202, 1997.
- Rathouz M and Trussell L.** Characterization of outward currents in neurons of the avian nucleus magnocellularis. *J Neurophysiol* 80: 2824–2835, 1998.
- Rothman JS and Manis PB.** Properties of a low-threshold potassium current in ventral cochlear nucleus neurons. *Soc Neurosci Abstr* 22: 647, 1996.
- Rothman JS and Manis PB.** Differential expression of three distinct potassium currents in the ventral cochlear nucleus. *J Neurophysiol* 89: 3070–3082, 2003a.
- Rothman JS and Manis PB.** Kinetic analyses of three distinct potassium conductances in ventral cochlear nucleus neurons. *J Neurophysiol* 89: 3083–3096, 2003b.
- Rothman JS and Young ED.** Enhancement of neural synchronization in computational models of ventral cochlear nucleus bushy cells. *Aud Neurosci* 2: 47–62, 1996.
- Rothman JS, Young ED, and Manis PB.** Convergence of auditory nerve fibers onto bushy cells in the ventral cochlear nucleus: implications of a computational model. *J Neurophysiol* 70: 2562–2583, 1993.
- Rudy B.** Diversity and ubiquity of K channels. *Neuroscience* 25: 729–749, 1988.
- Rusznak Z, Forsythe I, and Stanfield P.** Characterization of the hyperpolarization activated nonspecific cation current ( $I_h$ ) of bushy neurons from the rat anteroventral cochlear nucleus studied in a thin brain slice preparation. *Neurobiology* 4: 275–276, 1996.
- Ryugo DK and Sento S.** Synaptic connections of the auditory nerve in cats: relationship between endbulbs of held and spherical bushy cells. *J Comp Neurol* 305: 35–48, 1991.
- Sah P, Gibb AJ, and Gage PW.** The sodium current underlying action potentials in guinea pig hippocampal CA1 neurons. *J Gen Physiol* 91: 373–398, 1988.
- Schild JH and Kunze DL.** Experimental and modeling study of  $Na^+$  current heterogeneity in rat nodose neurons and its impact on neuronal discharge. *J Neurophysiol* 78: 3198–3209, 1997.
- Schwarz DW and Puil E.** Firing properties of spherical bushy cells in the anteroventral cochlear nucleus of the gerbil. *Hear Res* 114: 127–138, 1997.
- Travagli RA and Gillis RA.** Hyperpolarization-activated currents,  $I_h$  and  $I_{KIR}$ , in rat dorsal motor nucleus of the vagus neurons in vitro. *J Neurophysiol* 71: 1308–1317, 1994.
- Wang LY, Gan L, Forsythe ID, and Kaczmarek LK.** Contribution of the Kv3.1 potassium channel to high-frequency firing in mouse auditory neurons. *J Physiol* 509: 183–194, 1998.
- Wang X and Sachs MB.** Transformation of temporal discharge patterns in a ventral cochlear nucleus stellate cell model: implications for physiological mechanisms. *J Neurophysiol* 73: 1600–1616, 1995.
- White JA, Young ED, and Manis PB.** The electrotonic structure of regular-spiking neurons in the ventral cochlear nucleus may determine their response properties. *J Neurophysiol* 71: 1774–1786, 1994.
- Wu SH and Oertel D.** Intracellular injection with horseradish peroxidase of physiologically characterized stellate and bushy cells in slices of mouse anteroventral cochlear nucleus. *J Neurosci* 4: 1577–1588, 1984.
- Zhang S and Trussell LO.** A characterization of excitatory postsynaptic potentials in the avian nucleus magnocellularis. *J Neurophysiol* 72: 705–718, 1994.